Cyanobiphenyl-based liquid crystal dimers and the twist-bend nematic phase: on the role played by the length and parity of the spacer

Ewan Cruickshank[a], Grant J Strachan[a], Kamal Thapa[b,c], Damian Pociecha[d], Mirosław Salamończyk[d], John MD Storey[a], Ewa Gorecka[d], Oleg D. Lavrentovich[b,c,e] and Corrie T Imrie[a]*

[a]Department of Chemistry, School of Natural and Computing Sciences, University of Aberdeen, AB24 3UE, Scotland, United Kingdom; [b]Advanced Materials and Liquid Crystal Institute, Kent State University, Kent, Ohio 44242, USA; [c]Department of Physics, Kent State University, Kent, Ohio 44242, USA; [d]Faculty of Chemistry, University of Warsaw, ul. Zwirki i Wigury 101, 02-089, Warsaw, Poland; [e]Materials Science Graduate Program, Kent State University, Kent, Ohio 44242, USA

*Author for correspondence: email: c.t.imrie@abdn.ac.uk

ABSTRACT

Six members of the 1,ω-bis(4-cyanobiphenyl-4′-yl) alkanes are reported and referred to as CB*n*CB in which n = 1, 15, 16, 17, 19 and 20 and indicates the number of methylene units in the spacer separating the two cyanobiphenyl units. The behaviour of CB3CB is revisited. The temperature dependence of the refractive indices, optical birefringence, and dielectric permittivities measured in the nematic, N, phase for selected homologues are reported. The dimers with $n \geq 15$ showed an enantiotropic N phase, and for the odd members the twist-bend nematic, N_{TB}, phase was observed. CB3CB shows a direct N_{TB}-isotropic, I, transition whereas for CB1CB a virtual N_{TB}-I transition is found. The temperature dependence of the bend elastic constant, K_{33}, measured in the oblique helicoidal cholesteric state formed by mixtures of CB*n*CB with a chiral additive S811, shows strong non-monotonous behaviour with a deep minimum near the transition point to the N_{TB} phase. The minimum value of K_{33} decreases as n increases. The long even members of the CB*n*CB series show similar values of T_{NI} to their odd-membered counterparts but their estimated values of $T_{N_{TB}N}$ are considerably lower. This is attributed to molecular shape and its effect on K_{33}.

KEYWORDS

Twist-bend nematic phase; liquid crystal dimers; bend elastic constant; pitch length; helicoidal cholesteric phase; spacer.

1. Introduction

Over a decade has now passed since the first unambiguous assignment of the twist-bend nematic, N_{TB}, phase was made [1-3], and some fifty years since Meyer predicted its existence [4] and over twenty years since it was predicted independently by Dozov [5], both using symmetry arguments. A range of molecular structures have now been shown to exhibit the N_{TB} phase including odd-membered liquid crystal dimers [6-27] and higher oligomers [28-35], bent-core liquid crystals [36, 37], hydrogen-bonded supramolecular systems [38-42] and polymeric liquid crystals [43]. Recently an even-membered dimer containing a disulfide link in the spacer has been reported to exhibit the N_{TB} phase [44]. The common feature to each of these classes of materials is molecular bend, and this is wholly consistent with Dozov's seminal work [5]. He argued that bent structures have a strong natural tendency to pack into bent structures, but, given that pure uniform bend is not allowed in nature, it must be accompanied by another local deformation of the director. In the case of twist, this gives rise to the N_{TB} phase in which the director forms a heliconical distribution in which it is tilted with respect to the helical axis. The pitch of this helix is very short and typically just a few molecular lengths. A particularly fascinating feature of the N_{TB} phase is spontaneous symmetry breaking in a fluid system composed of achiral molecules and without positional order. Given that the formation of chirality is spontaneous equal numbers of left- and right-handed helices would be expected and hence, macroscopically the phase is achiral. The chiral N_{TB} phase may be obtained in which the double degeneracy of the helical twist sense has been removed either by the addition of chiral dopants [45] or by the introduction of intrinsic molecular chirality [46-48]. Dozov also predicted the existence of twist-bend smectic phases [5] and these have also been found experimentally [49-54].

The experimental discovery of the N_{TB} phase was made using CB7CB, a member of the 1,ω-bis(4-cyanobiphenyl-4′-yl) alkanes, the CB*n*CB series, see Figure 1(a). In CB7CB, seven methylene units separate the two cyanobiphenyl moieties, and this odd-membered spacer imparts the necessary molecular curvature to observe the N_{TB} phase. The CB*n*CB series contains three of the most extensively studied twist-bend nematogens; specifically, CB7CB, CB9CB and CB11CB (see, for recent examples, [55-67]). More widely, the overwhelming majority of twist-bend nematogens reported in the literature have either seven, nine or eleven atoms separating the mesogenic units. The reasons for this are two-fold: firstly, moving to shorter odd-membered spacers accentuates the molecular bend and tends to reduce the liquid crystal transition temperatures with respect to the melting point, and strongly monotropic materials are obtained [21, 68]. Secondly, and more pragmatically, moving to longer odd-

membered spacers is synthetically rather challenging. The CB*n*CB series is one of the most complete homologous series to be studied in terms of the spacer length, with values of *n* reported of 3, 5 - 11, and 13 [67, 69, 70]. Key questions remain, however, such as, what happens to the tendency to form the N_{TB} phase when the spacer becomes even shorter, or indeed very long? To address these issues, here we report the synthesis and characterisation of new members of the CB*n*CB series with *n* = 1, 15, 17 and 19, and revisit the behaviour for *n* = 3. In order to establish the dependence of the formation of the N_{TB} phase on molecular shape, and specifically, the bend angle of the dimer, we compare the transitional properties of the CB*n*CB series with those of the CBO*n*OCB series [71, 72], Figure 1(b). We also consider the difference in transitional behaviour between dimers having very long odd or even-membered spacers and report the synthesis and characterisation of members of the CB*n*CB series with *n* = 16 and 20.

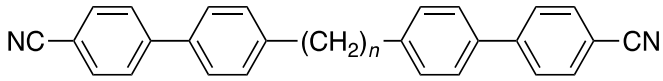

(a)

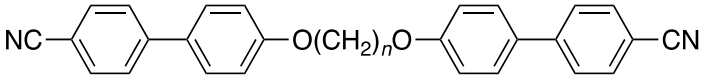

(b)

Figure 1. The general molecular structure of (a) the 1,ω-bis(4-cyanobiphenyl-4′-yl) alkanes, referred to as the CB*n*CB series and (b) the 1,ω-bis(4-cyanobiphenyl-4’-yloxy) alkanes, the CBO*n*OCB series. In both acronyms *n* refers to the number of methylene units in the flexible alkyl spacer.

To better understand the role of the spacer in determining the properties of these dimers, we also measure the temperature dependence of a number of material parameters, specifically the refractive indices, optical birefringence, and dielectric permittivities of the N phase formed by members of the CB*n*CB series with *n* = 7, 9, 11, 13, and 15. We also investigate the bend elastic constants, K_{33}, for these homologues. The very low values of K_{33} found in the nematic phases of odd-membered dimers [73] have been attributed to the bent-shape adopted by these dimers [74] and drive the formation of both the N_{TB} phase and also of the so-called oblique helicoidal cholesteric state, Ch_{OH}. Unfortunately, direct measurements of K_{33} in the N phase of the CB*n*CB dimers using the conventional technique involving a Frederiks transition in a homeotropic cell are problematic since the materials do not align homeotropically. Instead, we resort to measuring K_{33} in the chiral version of the N phase, the chiral nematic N* phase in

which the directors adopt a helical distribution and are perpendicular to the helical axis. When a N* phase formed by an odd-membered dimer is acted upon by an electric field, the small value of K_{33} yields an oblique helicoidal Ch_{OH} state [64, 75, 76], in which the local director is now tilted to the helical axis [75, 77]. In the Ch_{OH} state, the helical pitch P depends on K_{33} [75, 78, 79]; by measuring P using the electrically tuneable Bragg reflection of light, we may deduce K_{33}, as described previously [64, 77].

2. Experimental

2.1 Synthetic Methods

The synthesis of CB1CB is shown in Scheme 1. In the first step 4,4'-dibromobenzophenone was reduced using triethylsilane [67] to yield 1,1-bis(4-bromophenylmethane) (**1.1**) that was subsequently reacted with 4-cyanophenylboronic acid in a Suzuki-Miyaura cross-coupling reaction [80] to give CB1CB (**1.2**).

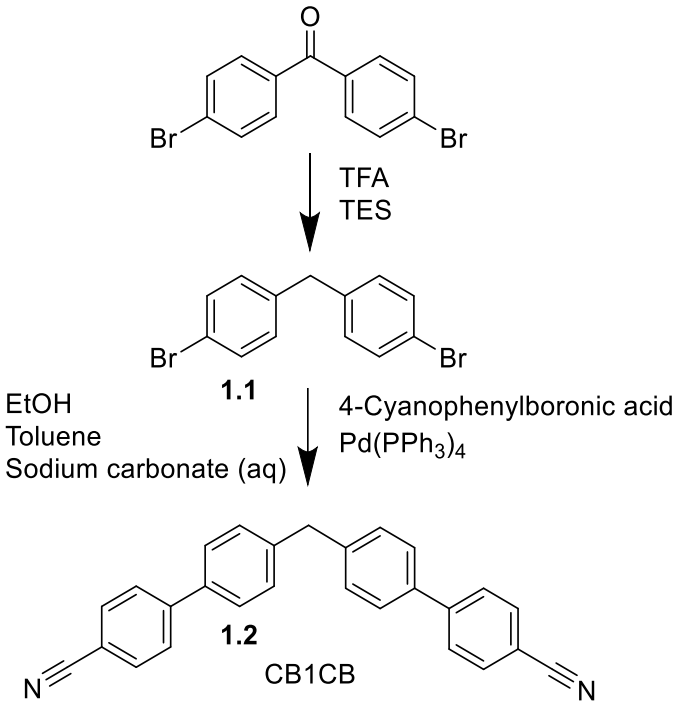

Scheme 1. Synthesis of CB1CB.

The synthesis of CB3CB followed the steps outlined in Scheme 2. In the first step, 2*E*-1,3-bis(4-bromophenyl)prop-2-en-1-one (**2.1)** was synthesised using a base catalysed aldol condensation between 4-bromobenzaldehyde and 4-bromoacetophenone.[81] **2.1** underwent a hydrosilane reduction [67] to form 1,3-bis(4-bromophenylpropane) (**2.2)** that was subsequently

reacted with 4-cyanophenylboronic acid in a Suzuki-Miyaura cross-coupling reaction [80] to form the desired product, CB3CB (**2.3**).

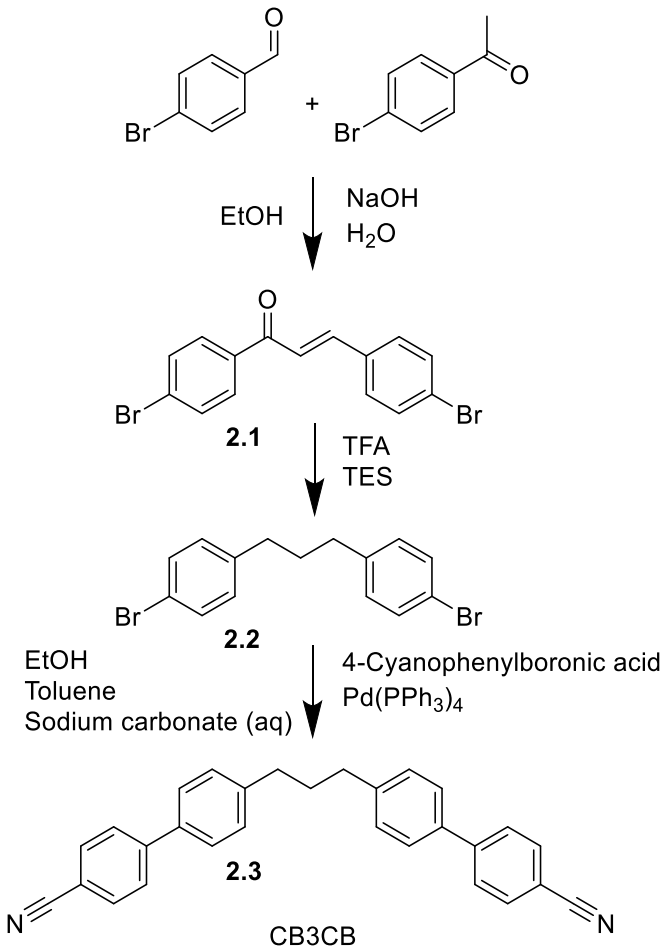

Scheme 2. Synthesis of CB3CB.

The synthesis of the extended chain alkanedioic acids required for the syntheses of the CB*n*CB homologues with long spacers is shown in Scheme 3 and based on the procedure reported by Obaza and Smith [82]. The synthesis of the CB*n*CB homologues having long spacers is shown in Scheme 4 and described elsewhere by Paterson *et al.*[67] A detailed description of the preparation of the members of the CB*n*CB series (*n*=1, 3, 15, 16, 17, 19, 20), including the structural characterisation data for all intermediates and final products, is provided in the Supplementary Information.

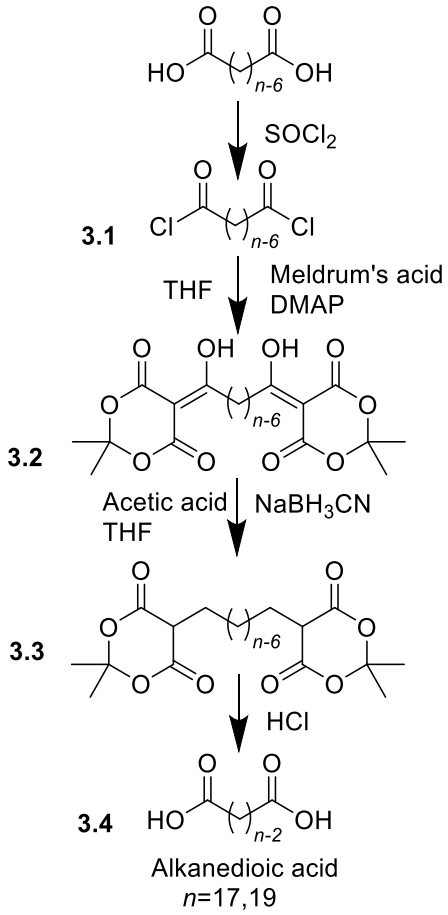

Scheme 3. Synthesis of extended alkanedioic acids.

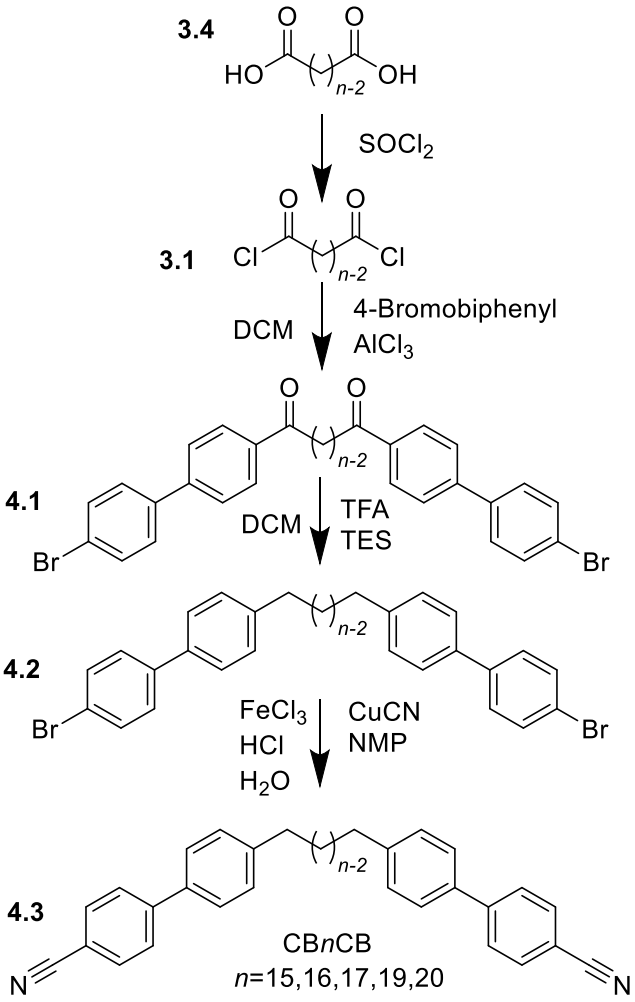

Scheme 4. Synthesis of the CB*n*CB series.

2.2 Thermal characterisation

Phase characterisation was performed by polarised light microscopy, using an Olympus BH2 polarising light microscope equipped with a Linkam TMS 92 hot stage. The untreated glass slides were approximately 0.17 mm thick. The cells treated for planar alignment were purchased from INSTEC, they were 2.9-3.5 μm thick and possessed transparent ITO electrodes.

The phase behaviour of the materials was studied by differential scanning calorimetry performed using a Mettler Toledo DSC1 or DSC3 differential scanning calorimeter equipped with TSO 801RO sample robots and calibrated using indium and zinc standards. Heating and cooling rates were 10 K min^{-1}, with a 3-min isotherm between either heating or cooling, and all samples were measured under a nitrogen atmosphere. Transition temperatures and associated enthalpy changes were extracted from the heating traces unless otherwise noted.

2.3 Molecular modelling

The geometric parameters of the CB*n*CB series were obtained using quantum mechanical DFT calculations with Gaussian09 software.[83] Optimisation of the molecular structures was carried out at the B3LYP/6-31G(d) level. Visualisations of electronic surfaces and ball-and-stick models were generated from the optimised geometries using the GaussView 5 software.[84] The electronic surfaces were found with the cubegen utility in GaussView by generating a total density cube using a SCF density matrix and course grid, overlayed by an ESP surface map. Visualisations of the space-filling models were produced post-optimisation using the QuteMol package.[85]

2.4 Resonant X-ray scattering

The resonant x-ray scattering measurements were performed at the Advanced Light Source, Lawrence Berkeley National Laboratory on the soft x-ray beam line (11.0.1.2). The energy of incident beam was tuned to the K-edge of carbon absorption (283 eV). Samples with thickness lower than 1 μm were prepared between SiN membranes. The scattering intensity was recorded using the Princeton PI-MTE CCD detector.

2.5 Refractive indices and birefringence of the N phase

The temperature dependence of the ordinary (n_o) and extra-ordinary (n_e) refractive indices were determined by investigating light interference in wedge cells [86]. The measurements were performed at the wavelengths 488 nm, 532 nm, and 632.8 nm, using laser-line colour filters with a central bandwidth of 1 nm (Thorlabs, Inc.). The wedge cells of a small dihedral angle < 1˚ were constructed using glass plates coated with a polyimide PI 2555, which is rubbed along the direction perpendicular to the thickness gradient to prevent director deformations. The temperature dependencies of the birefringence, $\Delta n(T)$ were determined by measuring the optical retardance $\Gamma(T) = \Delta n(T)d$, in rubbed PI2555 planar cells of thicknesses d = (3.9-4.2) μm, using a MicroImager (Hinds Instruments) at the wavelength 535 nm.

2.6 Dielectric anisotropy of the N phase

The dielectric permittivities were determined in thin rubbed PI2555 planar cells of a thickness d = (3.9-4.2) μm with square ITO electrodes of area 5 mm × 5 mm at a frequency of 3 kHz, using capacitance measurements with a 4284A LCR meter (Hewlett Packard). The

perpendicular permittivity $\varepsilon_{\perp}(T)$ was measured at a low applied voltage of 0.1 V that does not perturb the homogeneous planar structure whereas the parallel permittivity $\varepsilon_{\parallel}(T)$ was measured in the same planar cell using an extrapolation method at high applied voltage that aligns the molecules perpendicularly to the electrodes [87].

2.7 Bend elastic constant in the oblique helicoidal state (Ch_{OH})

2.7.1 Preparation and characterisation of the chiral mixtures

The binary mixtures of the CB*n*CB dimers, *n* = 7, 9, 11, 13, and 15, with the left-handed chiral additive S811 (EM Industries), CB*n*CB: S811 = 96:4 (wt.%), were studied in ITO PI 2555 planar cells of thickness *d* = (19.5-19.7) μm; the larger thickness ensures strong Bragg reflection from the Ch_{OH} state. The phase transition temperatures were determined by observing the optical textures under the polarizing optical microscope, a Nikon OPTIPHOT2-POL (Nikon Inc.) equipped with an QImaging camera, on cooling from the isotropic phase at 0.1 K min^{-1}. The temperature was controlled using a HCS302 hot stage connected to a mK2000 controller (Instec, Inc.) with an accuracy of ±0.01 K.

2.7.2 Bend elastic constant in the oblique helicoidal state (Ch_{OH})

The temperature dependencies of the bend elastic constant K_{33} for the dimers were measured in the oblique helicoidal state (Ch_{OH}) using the chiral mixtures described in section *2.7.1*. The Ch_{OH} state was obtained by applying an external sinusoidal ac voltage of frequency 3 kHz to ITO-covered planar cells of thickness d = (19.5-19.7) μm [75, 76]. The ac sinusoidal signal was produced by a SDG 1032X (SIGLENT Technologies) waveform generator, and amplified by a 7602M (KROHN-HITE Co.) voltage amplifier. The applied voltage was measured using a KEITHLEY 2000 multimeter. A tungsten halogen light source, LS-1 (360-2000 nm), and a USB2000 fiber optics spectrometer (both Ocean Insight) were used to characterize the Bragg reflection. The unpolarized light from the LS-1 light source was passed through a UV-VIS bifurcated optical fiber (200 μm diameter) and was incident normally on the Ch_{OH} cells. The superimposed reflected beam from the Ch_{OH} cells passed through the same bifurcated optical fiber and detected using the USB2000 spectrometer interfaced with OceanView spectroscopy software (Ocean Insight). The well-equilibrated reflection spectra at each temperature point of interest, above the N*-N_{TB}* transition temperature, were recorded as a function of the applied electric field *E*.

3. Results and Discussion

3.1 Phase behaviour

The transitional properties of the new members of the CB*n*CB series reported here are listed in Table 1. All the long homologues ($n \geq 15$) exhibit an enantiotropic conventional nematic phase identified on the basis of the textures observed using polarised light microscopy. Specifically, when sandwiched between two untreated glass slides, a characteristic schlieren texture was observed containing both two- and four-point brush singularities and which flashed when subjected to mechanical stress, see Figure 2(a). On cooling the odd members (n = 15, 17, 19), a blocky schlieren texture developed, see Figure 2(b), and this was accompanied by the cessation of the optical flickering associated with director fluctuations in the N phase. These changes are characteristic of a N-N_{TB} phase transition. For CB15CB, the N_{TB} phase is enantiotropic whereas for CB17CB and CB19CB it is marginally monotropic in nature. The long even-membered homologues (n = 16, 20) show an enantiotropic conventional nematic phase and the absence of the N_{TB} phase is consistent with the widely held view that molecular curvature is a prerequisite for its observation. We return to this theme later.

Table 1. Transition temperatures and associated scaled entropy changes for the CB*n*CB series.

n	$T_{Cr\text{-}}$/ °C	$T_{N_{TB}N}$/ °C	$T_{N_{TB}I}$/ °C	T_{NI}/ °C	$\Delta S_{Cr\text{-}}/R$	$\Delta S_{NI}/R$
1	206	-	−3 [b]	-	7.43	-
3	141	-	47 [c]	-	8.29	-
15	96	103	-	121	13.5	1.50
16	111	-	-	132	13.4	2.17
17	99	97 [a]	-	117	15.3	1.45
19	99	95 [a]	-	115	16.7	2.20
20	115	-	-	116	15.3	1.76 [a,d]

[a]Values extracted from DSC cooling traces. [b]Virtual transition temperature estimated from a binary phase diagram with CB7CB. [c]Measured using the polarised light microscope. [d] The peak associated with the N-I transition overlaps that associated with crystallisation on cooling and with melting on heating, and this value underestimates $\Delta S_{NI}/R$.

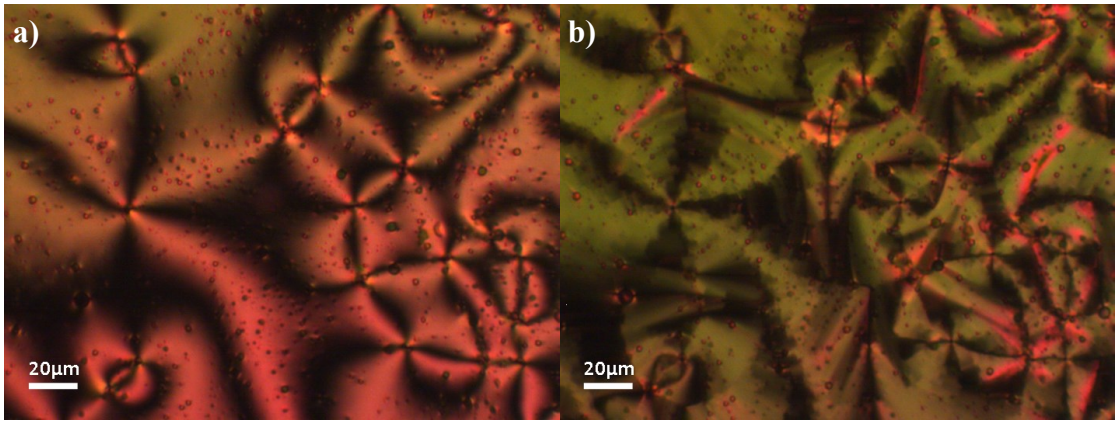

Figure 2. (a) The schlieren texture seen for the N phase (T = 114 °C) and (b) the blocky schlieren texture of the N_{TB} phase (T = 95 °C) observed for CB19CB.

The N_{TB} phase exhibited by CB15CB was also characterised using resonant soft X-ray scattering (RSoXS) The diffraction signal under the resonance condition is sensitive to the orientation of the molecules unlike conventional XRD. Figure 3(a) shows the temperature evolution of the resonant XRD signal recorded in the N_{TB} phase, and Figure 3(b) the temperature dependence of the measured pitch length. The values of the pitch length decrease from around 300 Å at the N_{TB}-N transition to around 150 Å on cooling. These values are much higher than previously measured for members of the CB*n*CB series; for example, the pitch length measured in the N_{TB} phase for CB7CB is around 80 Å.[2, 3, 88] If we assume that the helical structure in the N_{TB} phase does not change with spacer length then the increased pitch length may reflect, at least in part, the increase in molecular length from 26.2 Å for CB7CB to 36.4 Å for CB15CB. This increase in molecular length in itself, however, does not appear sufficiently large to account for a doubling of the pitch length. A strong dependence of the pitch length on increasing the spacer length from seven to eleven methylene units in a series of fluorinated dimers was reported by Saha *et al.* [89] and attributed to differences in the molecular bend angle between the two dimers in the N_{TB} phase. It has also been reported that changes in shape arising from inverting an ester linkage connecting the spacer to the mesogenic units in a dimer doubled the pitch length in the N_{TB} phase although the molecular length was changed by a much smaller amount [90]. These changes also influence the bend elastic constant, K_{33}, to be discussed later, and this may contribute to the increase in pitch length on increasing spacer length.

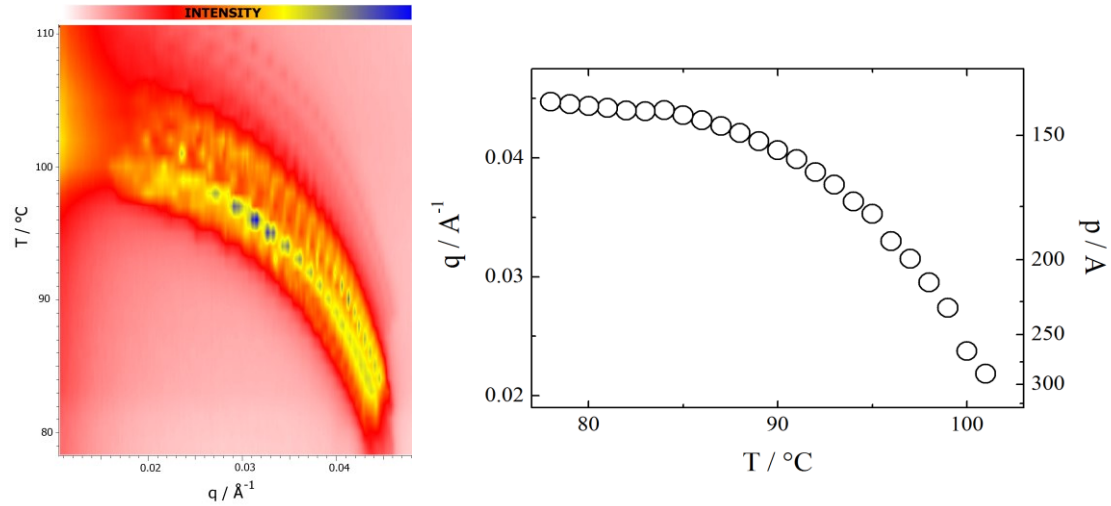

(a) (b)

Figure 3 (a) Temperature evolution of the resonant soft X-ray diffraction signal in the N_{TB} phase measured on cooling, and (b) the temperature dependence of the pitch length measured in the N_{TB} phase on cooling for CB15CB.

CB3CB melted directly into the isotropic liquid. On cooling, a strongly monotropic, reversible phase transition was observed at 47 °C. The texture associated with this phase appeared to consist of focal conic fans when viewed under the polarised optical microscope, but the textures obtained were rather ill distinct for samples both sandwiched between untreated slides and in 3-micron cells treated for planar alignment, see Figure 4. The strongly monotropic nature of the phase precluded its study using X-ray diffraction. In order to assign this phase, a phase diagram was constructed using binary mixtures of CB3CB and the standard twist-bend nematogen, CB7CB [1], see Figure 5. Complete miscibility was observed over the entire range of compositions studied. The DSC traces obtained on cooling the mixtures are shown in Figure 6. For mixtures containing ≥ 70 mol % CB7CB, the phase sequence N_{TB}-N-I was observed. For the 80 and 90 mol % CB7CB mixtures, exotherms associated with each transition are observed whereas for the 70 mol % mixture the nematic range is too short, and only a single broad exotherm is seen in the trace shown in Figure 6. Again, the N phase was identified on the basis of the observation of a characteristic schlieren texture, Figure 7(a), and the N_{TB} phase assigned by the observation of a focal conic fan texture, Figure 7(b). As noted earlier, the N-N_{TB} phase transition was associated with the cessation of the optical flickering seen in the N phase. For the mixtures containing ≤ 60 mol % CB7CB, a direct N_{TB}-I transition was observed,

and just a single endotherm is observed in the DSC traces, see Figure 6. The optical textures observed for the N_{TB} phase included both focal conic fan and polygonal textures, Figures 7(c) and 7(d), respectively. The focal conic fan texture arises from the pseudo-layered structure of the N_{TB} phase associated with the pitch length. The N-I phase transition temperature in the CB3CB:CB7CB phase diagram decreases linearly on increasing the mole fraction of CB3CB suggesting that the intermolecular energy parameter between the unlike species is the geometric mean of the interaction parameters between the like species [91]. This is an unsurprising result given the similar molecular structures of the two components. The line connecting the N_{TB}-N and N_{TB}-I transition temperatures also shows a linear dependence on increasing the concentration of CB3CB. The gradient of the N-I line is greater than that of the N_{TB}-N/I line, and these intercept at around 62 mol% CB7CB, see Figure 5. Critically, the transition temperature measured for pure CB3CB lies on the N_{TB}-N/I line indicating that the transition described earlier is indeed a direct N_{TB}-I transition and confirms that the textures shown in Figure 3 are examples of the natural textures of the N_{TB} phase for a pure compound. This is particularly noteworthy given that N_{TB}-I transitions in pure materials have been observed only rarely [7, 8, 13, 70, 92, 93]. The transitional behaviour reported here for CB3CB agrees well with that reported in the literature by Arakawa and co-workers who based their N_{TB} phase assignment solely on optical textures [70]. An earlier report of the CB3CB overlooked the monotropic liquid crystalline behaviour reported here [69].

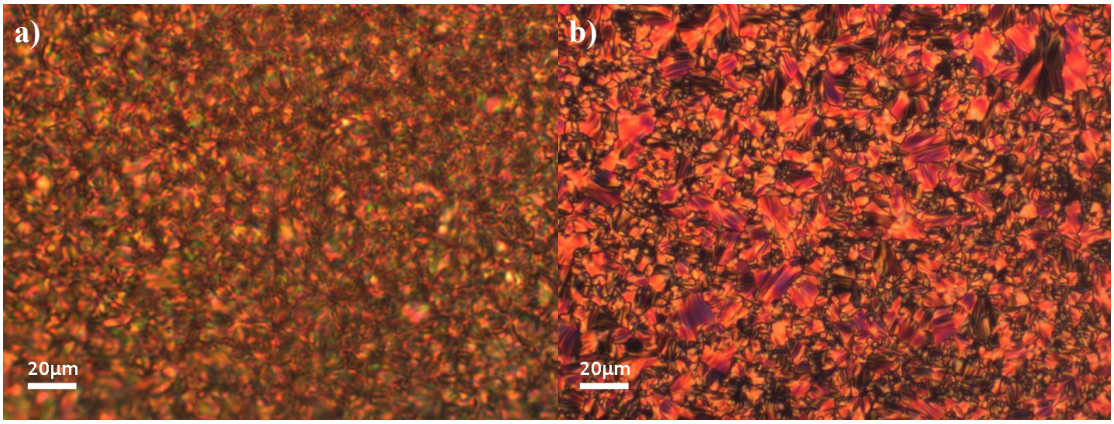

Figure 4. Optical textures observed on cooling CB3CB: (a) between untreated slides, a poorly defined fan-like texture (T = 43 °C); (b) in a 3 µm cell treated for planar alignment, a focal conic fan texture (T = 45 °C). These are examples of the natural textures of the N_{TB} phase.

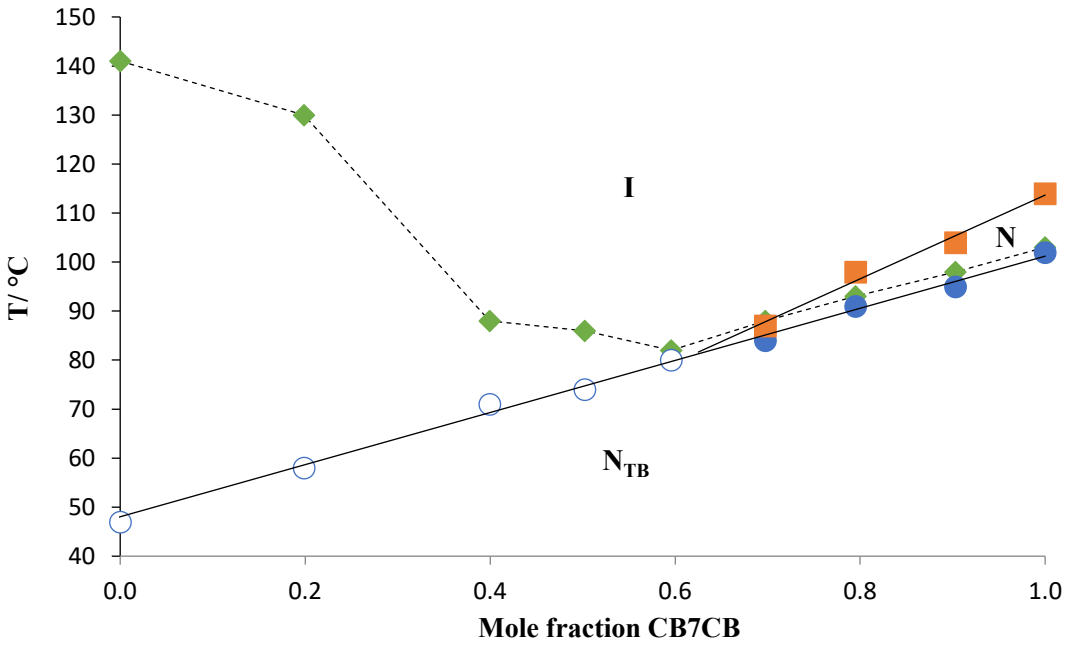

Figure 5. Phase diagram constructed for binary mixtures of CB3CB and CB7CB. Squares denote T_{NI}, filled circles $T_{N_{TB}N}$, open circles $T_{N_{TB}I}$ and diamonds the melting points.

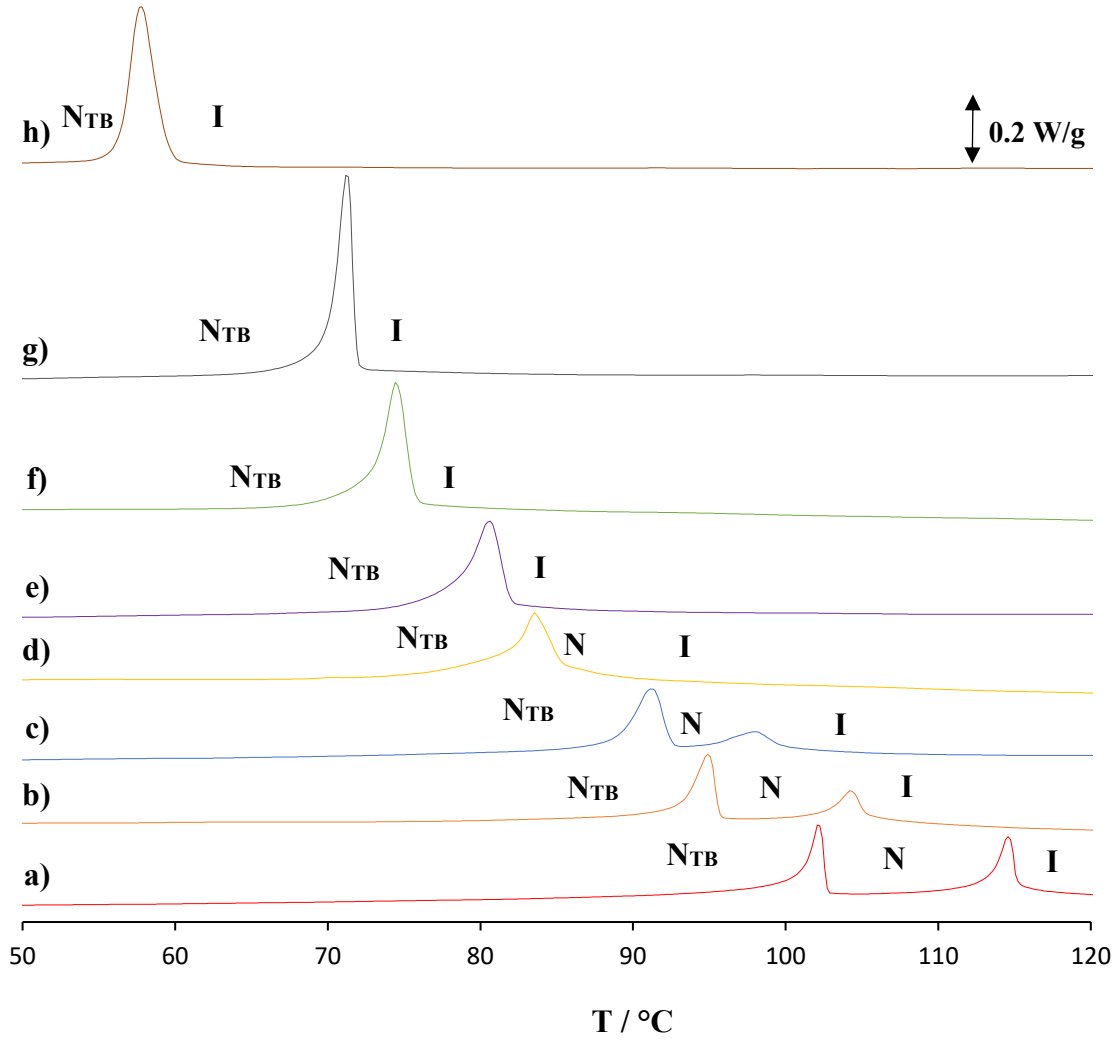

Figure 6. DSC traces obtained on cooling from the isotropic phase for: (a) CB7CB; and for the CB7CB:CB3CB mixtures (b) 90:10; (c) 80:20; (d) 70:30; (e) 60:40; (f) 50:50; (g) 40:60; (h) 20:80 mol %. The crystallisation exotherms are not shown.

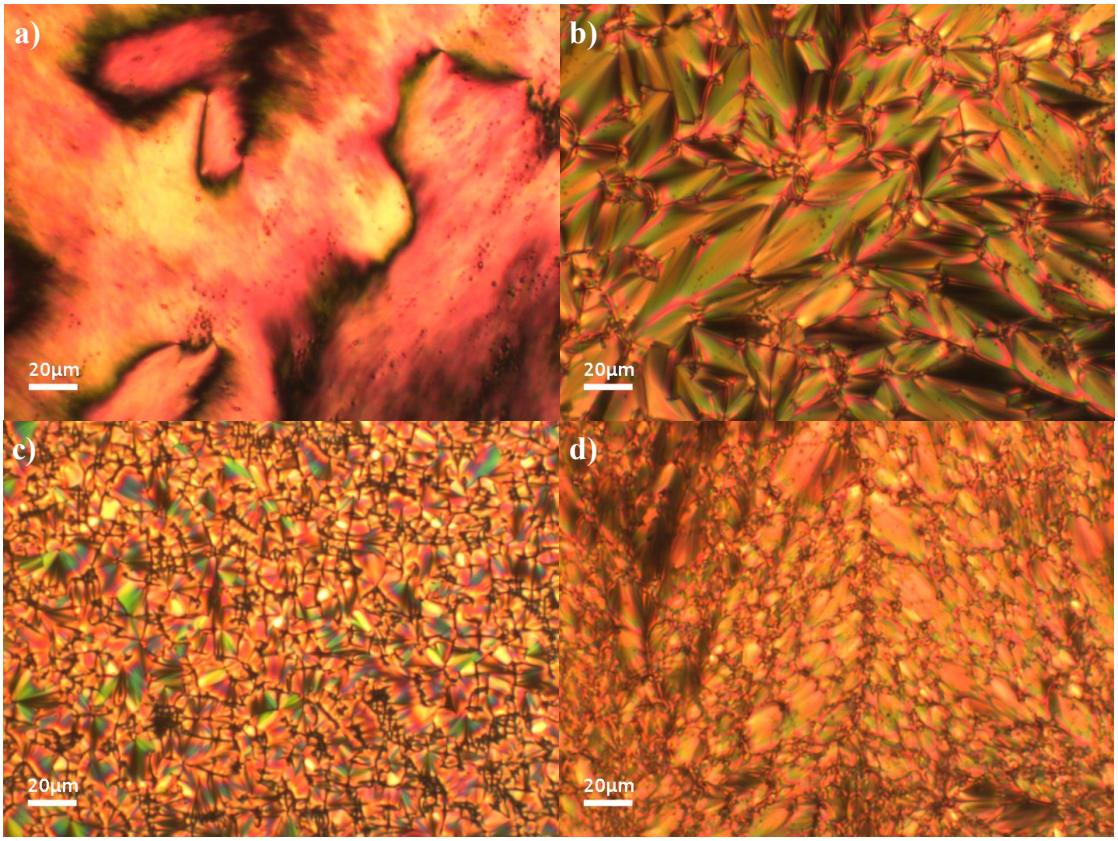

Figure 7. Optical textures observed for CB7CB:CB3CB mixtures: (a) schlieren texture of the N phase (T = 101 °C) and (b) focal conic texture of the N_{TB} phase (T = 94 °C) shown by the 90:10 mol % mixture; (c) focal conic texture of the N_{TB} phase (T = 65 °C) seen for the 60:40 mol % mixture; (d) focal conic texture of the N_{TB} phase (T = 58 °C) shown by the 20:80 mol % mixture.

CB1CB also melted directly into the isotropic phase and on cooling, crystallised without showing any other liquid crystal phase behaviour. In order to determine a virtual I-N_{TB} transition temperature for CB1CB, a phase diagram was constructed using binary mixtures of CB1CB and CB7CB [1], see Figure 8. Miscibility was observed over the composition range for which liquid crystallinity was observed. The DSC traces obtained on cooling the mixtures that exhibited liquid crystallinity are shown in Figure 9. The mixtures containing ≥ 80 mol % CB7CB exhibited N_{TB} and N phases whereas those containing ≤ 70 mol % CB7CB showed a direct N_{TB}-I transition. These transitions were identified using polarised light microscopy, see Figure 10, and included the observation of a rope-like texture the formation of which was attributed to the undulation of pseudolayers during the temperature-induced shrinkage of the

N_{TB} pitch, [94, 95]. As also seen in the CB3CB:CB7CB phase diagram (Figure 5), the N-I and N_{TB}-N/I lines both show a linear dependence on increasing the concentration of CB1CB, and the N-I line has the larger gradient, intersecting the N_{TB}-N line at around 70 mol % CB7CB (Figure 8). The CB1CB:CB7CB mixtures first show a direct N_{TB}-I transition at a lower concentration of CB1CB than seen for CB3CB in the mixtures of CB3CB:CB7CB. This presumably reflects the more bent structure of CB1CB. The mixtures containing ≤ 50 mol % CB7CB did not show liquid crystalline behaviour, and this may be attributed, at least in part, to the sigmoidal dependence of the melting points of the mixtures on the concentration of CB1CB, and their dramatic increase below 60 mol % CB7CB (Figure 8). The virtual value of $T_{N_{TB}I}$ estimated for CB1CB is −3 °C although we note that this is obtained from a rather long extrapolation of the N_{TB}-N/I line and so must be treated with some degree of caution (Figure 8).

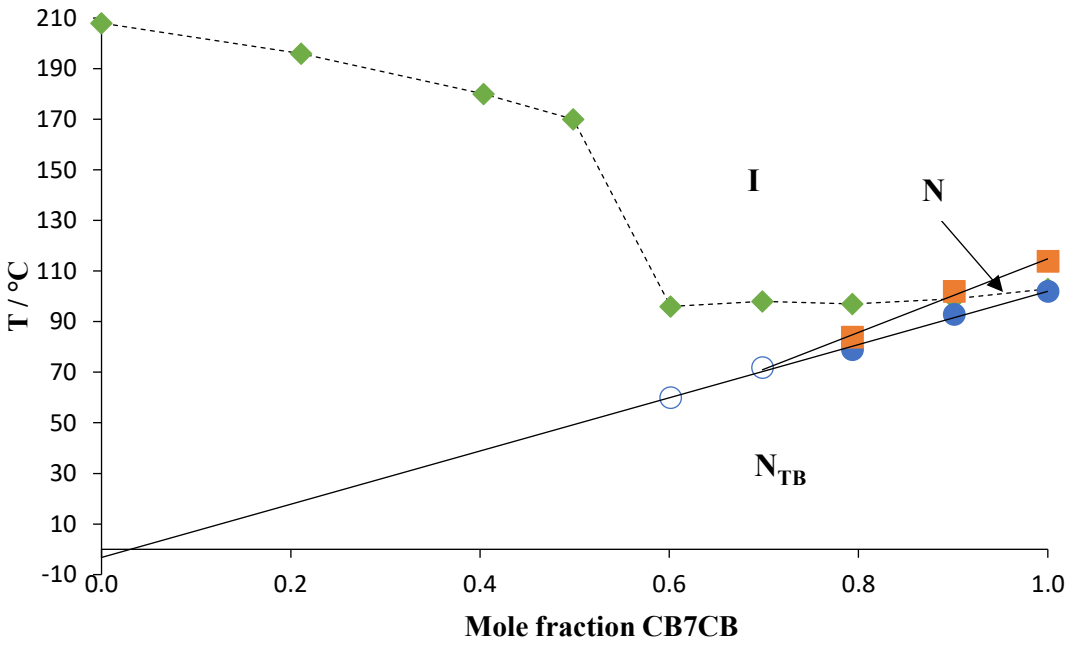

Figure 8. Phase diagram constructed for binary mixtures of CB1CB and CB7CB. Squares denote T_{NI}, filled circles $T_{N_{TB}N}$, open circles $T_{N_{TB}I}$ and diamonds the melting points.

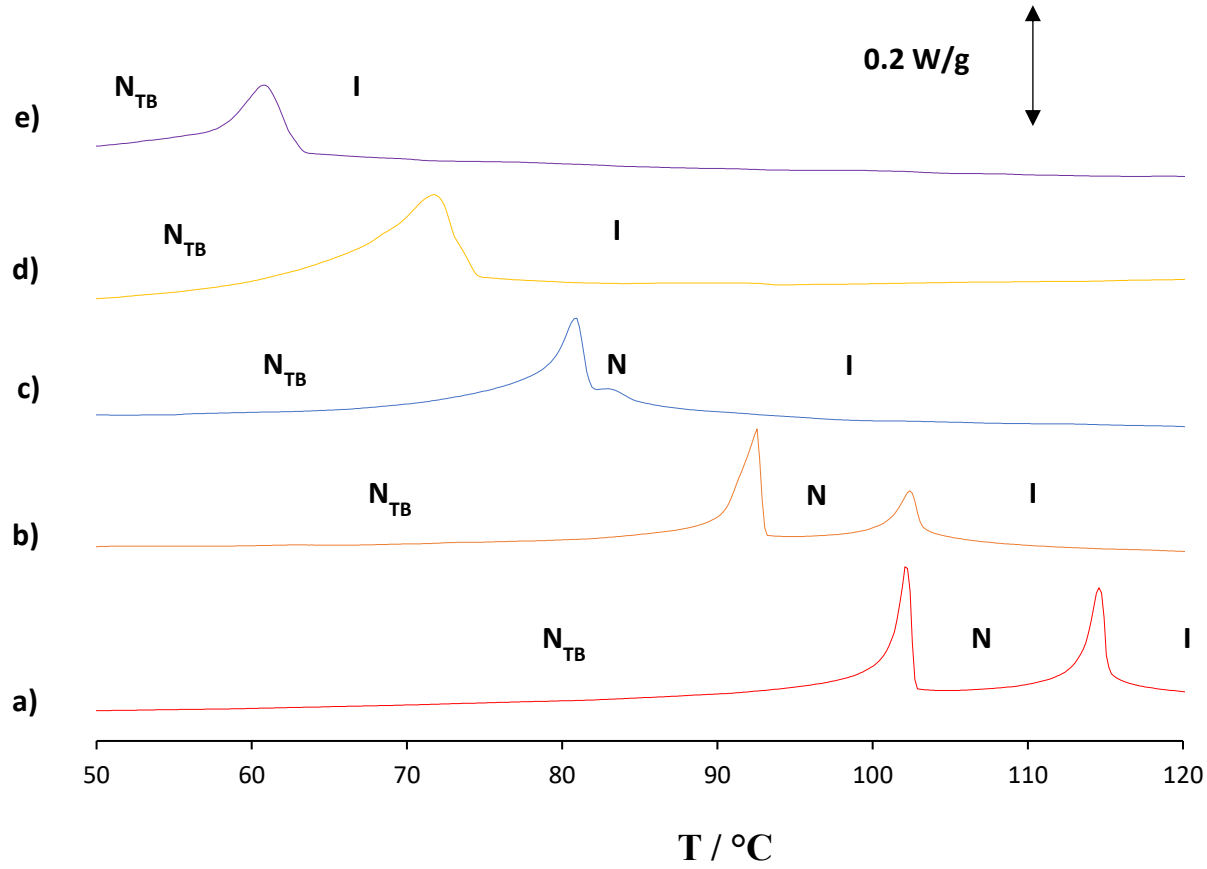

Figure 9. DSC traces obtained on cooling from the isotropic phase for: (a) CB7CB; and for the CB7CB:CB1CB mixtures (b) 90:10; (c) 80:20; (d) 70:30; (e) 60:40 mol %. The crystallisation exotherms are not shown.

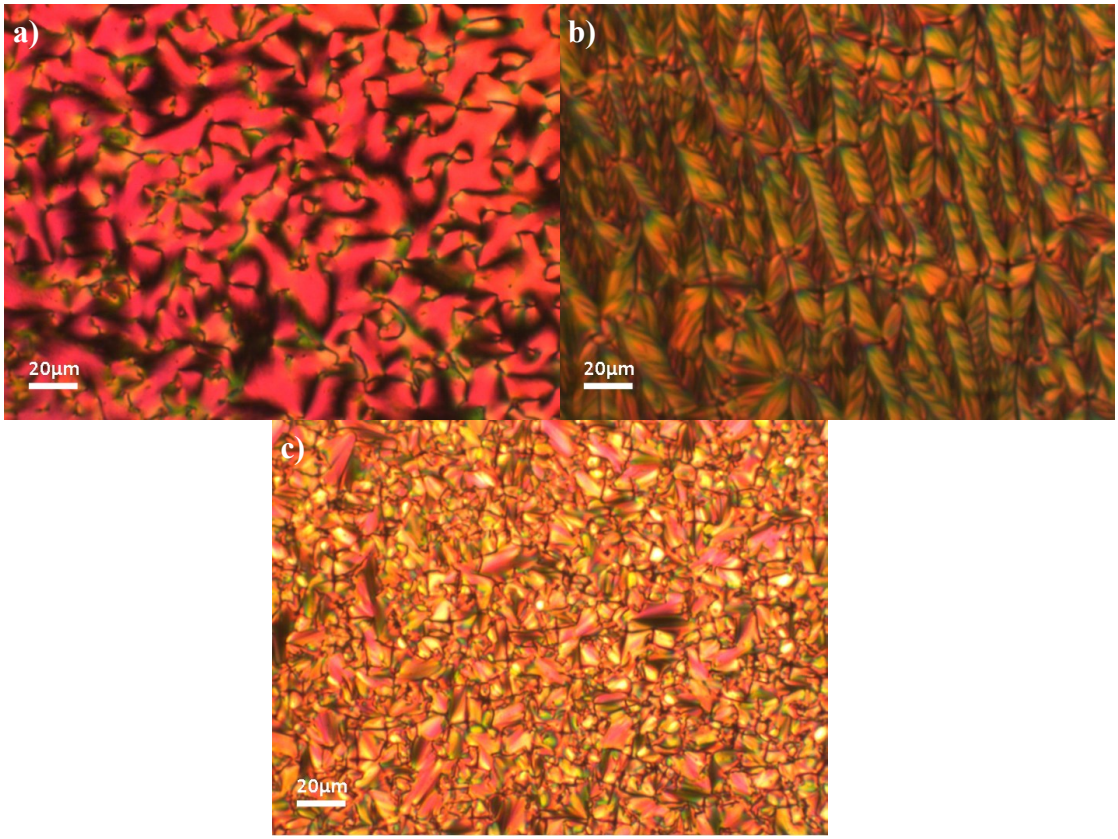

Figure 10. Optical textures observed for the CB7CB:CB1CB mixtures: (a) schlieren texture of the N phase (T = 85 °C) and (b) rope-like texture of the N_{TB} phase with undulating pseudolayers (T = 60 °C) shown by the 80:20 mol % mixture; (c) the natural focal conic fan texture of the N_{TB} phase obtained by cooling the isotropic phase (T = 74 °C) for the 60:40 mol % mixture.

The dependence of the transition temperatures on the length of the flexible spacer for the odd members of the CB*n*CB series is shown in Figure 11. The melting points decrease initially on increasing *n* before appearing to reach a limiting value. The first two odd members (*n* = 1, 3) show N_{TB}-I transitions, whereas CB5CB shows a narrow temperature range N phase in addition to the N_{TB} phase. The transition temperatures ($T_{N_{TB}I}$, $T_{N_{TB}N}$ or T_{NI}) increase sharply over the first three members of the series (*n* = 1, 3, 5). Further increasing *n* sees the values of both $T_{N_{TB}N}$ and T_{NI} pass through weak maxima for CB11CB, and begin to decrease, albeit very slowly. The temperature range of the N phase remains approximately constant for the higher values of *n*. We will return to a discussion of the trends in transition temperatures seen in Figure 10 later.

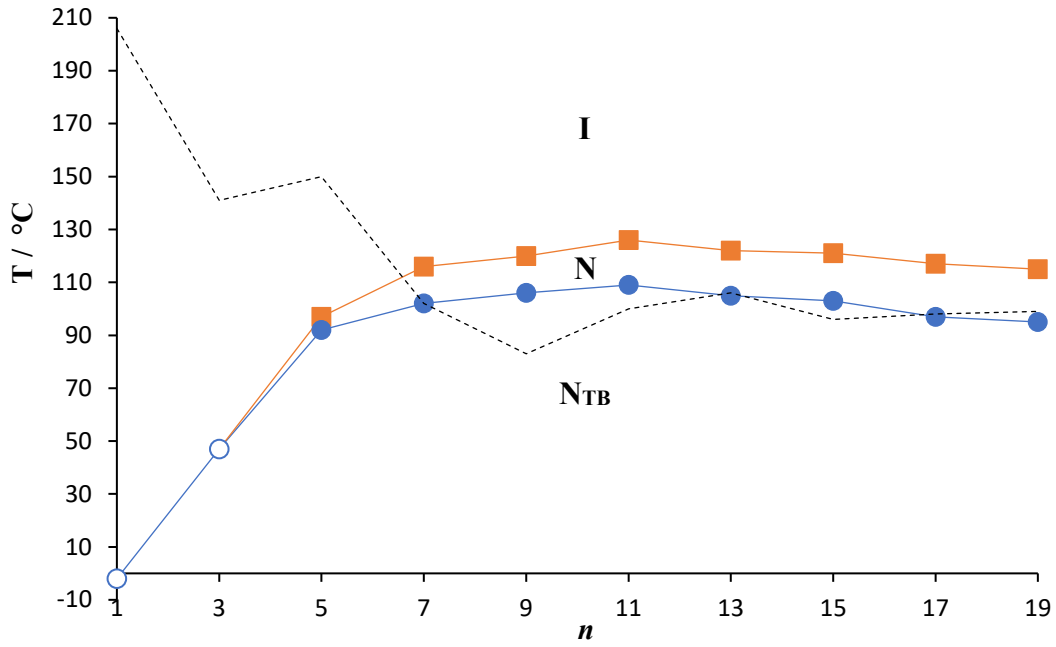

Figure 11. The dependence of the transition temperatures on the length of the alkyl spacer, n, for the odd members of the CBnCB series. The squares denote T_{NI}, the empty circles $T_{N_{TB}I}$, and the filled circles $T_{N_{TB}N}$. The broken line connects the melting points.

3.2 Refractive indices and birefringence

We now turn our attention to the material properties of these dimers. The temperature dependences of the extraordinary n_e and ordinary n_o refractive indices for CB13CB over the entire temperature range of the nematic phase are shown in Figure 12. Figures 13(a,b,c) presents the temperature dependencies of n_o for all CBnCB homologues, n = 7, 9, 11 and 15, over the temperature range $0 \leq T\text{-}T_{NN_{TB}} \leq 6$ ˚C, for three different wavelengths. The ordinary refractive index n_o for all five dimers shows a very weak temperature dependence, in agreement with the previous measurements reported for CB7CB and CB11CB [64]. As the molecular length increases, n_o decreases, Figures.13(d,e,f); a similar trend has been reported for the cyanobiphenyl monomers by Sarkar *et al*. [96].

The temperature dependence of the birefringence, $\Delta n(T)$, for the N phase of the CBnCB dimers, deduced from the measurements of optical retardance in flat planar cells, is shown in Figure 14. The measured value of $\Delta n(T)$ for CB13CB is consistent with the wedge cell data, Figure 12. The birefringence $\Delta n(T)$ increases as n increases from 7 to 15, and this may be attributed to the higher optical polarizability of longer molecules [97]. A similar trend is seen for fluorinated dimers that also form the N_{TB} phase [98]. On the other hand, the trend is opposite

to the behaviour observed in conventional monomeric cyanobiphenyls, in which the birefringence decreases in higher homologues with longer aliphatic terminal chains [96]. On cooling from the isotropic phase, $\Delta n(T)$ increases for all the dimers as the orientational order increases with decreasing temperature. As the temperature is reduced towards the N-N_{TB} transition, $\Delta n(T)$ behaves differently in different homologues: (i) Δn increases for CB7CB, as reported by Meyer *et al* [99], and CB9CB; (ii) Δn saturates for CB11CB; (iii) Δn slightly decreases for CB13CB and CB15CB. The pretransitional decrease of $\Delta n(T)$ close to the N-N_{TB} transition is observed for other flexible dimers [2, 98, 100, 101].

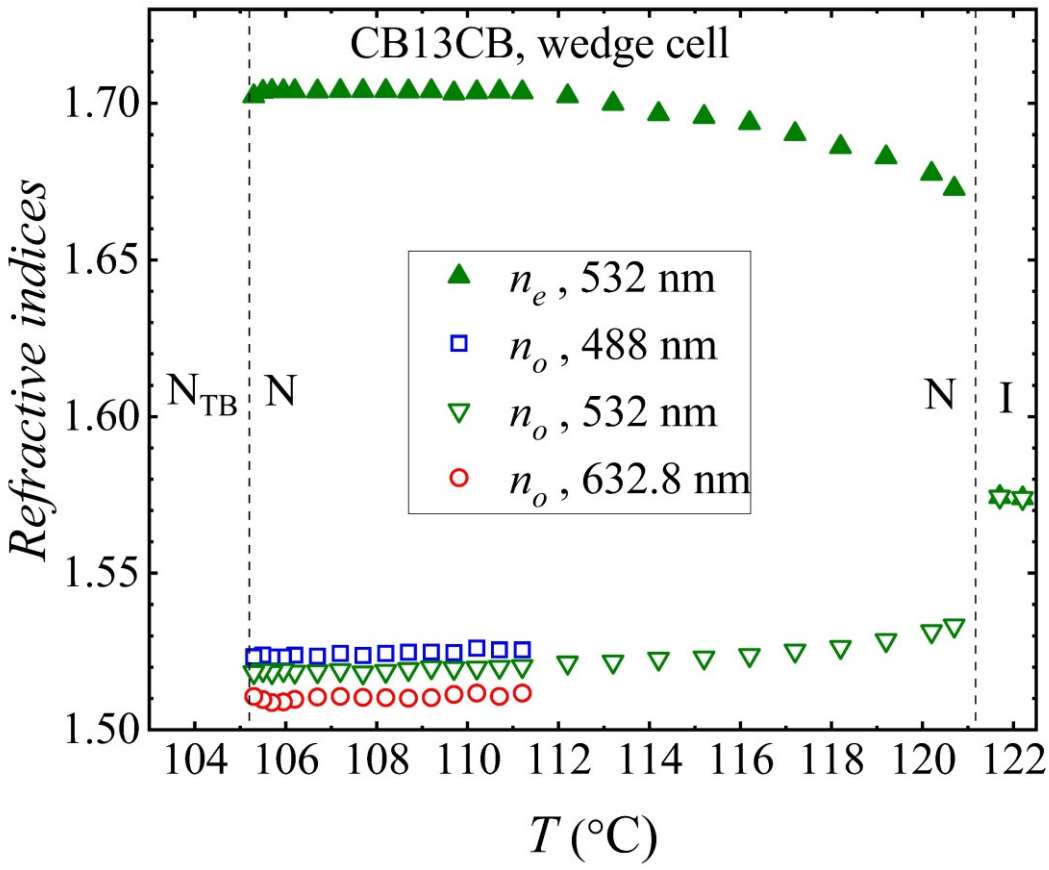

Figure 12. Temperature dependence of extraordinary refractive index n_e at 532 nm and ordinary refractive index n_o at 488 nm, 532 nm, and 632.8 nm for CB13CB in a wedge cell.

3.3 Dielectric anisotropy

The temperature dependencies of the dielectric permittivities measured when the electric field is parallel to the director, $\varepsilon_{\parallel}(T)$, and perpendicular to it, $\varepsilon_{\perp}(T)$, are plotted in Figures 15(a-e). Figure 15(f) shows that $\varepsilon_{\perp}$ decreases substantially as the molecular length

increases, while $\varepsilon_{\parallel}$ shows a much weaker dependence on n. As a result, the dielectric anisotropy $\Delta\varepsilon(T)$, which is positive for all homologues, increases as the flexible alkyl spacer increases in length, Figure 16, similar to the behaviour seen for $\Delta n(T)$ in Figure 14. The same trend is observed for the absolute value of the negative $\Delta\varepsilon(T)$ measured in fluorinated dimers [98]; however, conventional monomeric cyanobiphenyls show an opposite behaviour, as $\Delta\varepsilon(T)$ decreases in homologues with a longer aliphatic end chains [96]. As a function of temperature, $\Delta\varepsilon(T)$ is weakly non-monotonous, decreasing as the temperature approaches the transition points to the isotropic phase and to the N_{TB} phase, Figure 16; the latter can be attributed to the formation of pretransitional clusters with twist-bend molecular arrangements.

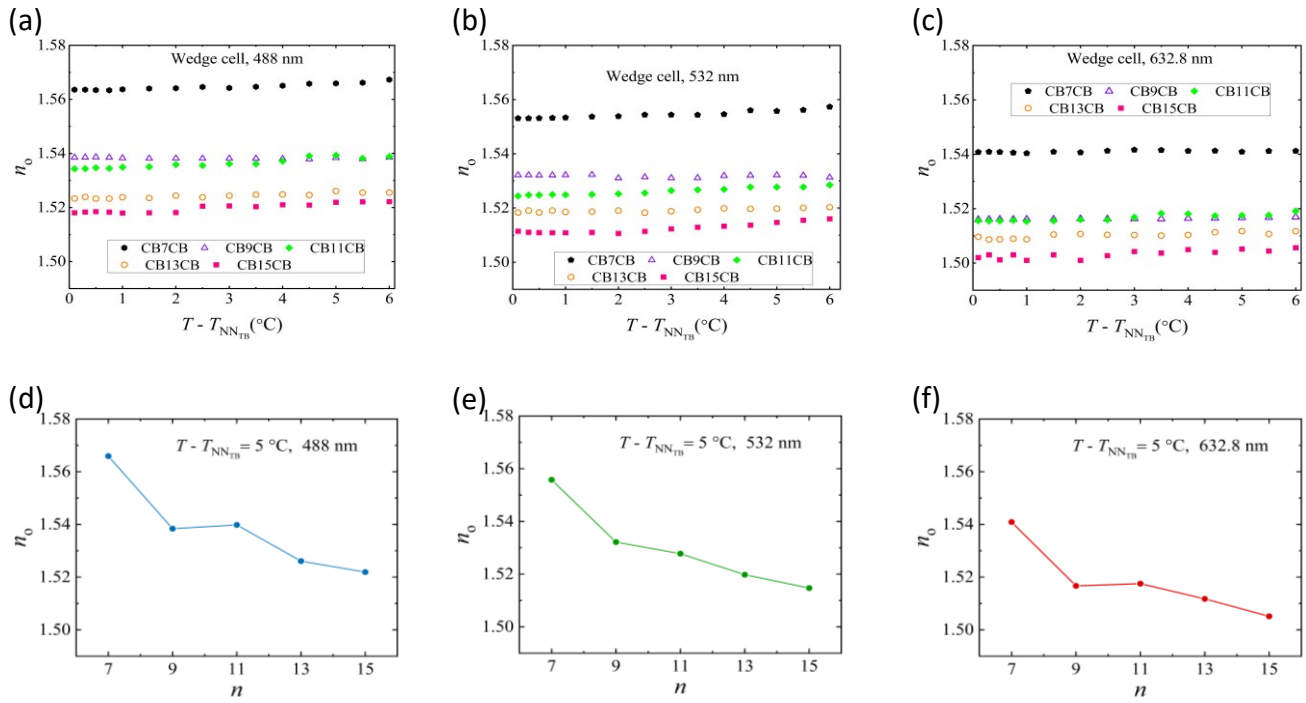

Figure 13. Temperature (a,b,c) and molecular length (d,e,f) dependencies of the ordinary refractive index n_o for CBnCB dimers in the range $0 \leq T\text{-}T_{NN_{TB}} \leq 6$ ˚C at wavelengths (a,d) 488 nm, (b,e) 532 nm, and (c,f) 632.8 nm. The error bars are smaller than the size of the plot symbols. The reference transition temperatures are $T_{NN_{TB}} = 102.2$°C for $n = 7$, $T_{NN_{TB}} = 106.4$°C for $n = 9$, $T_{NN_{TB}} = 107.9$°C for $n = 11$, $T_{NN_{TB}} = 105.2$°C for $n = 13$ and $T_{NN_{TB}} = 101.3$°C for $n = 15$.

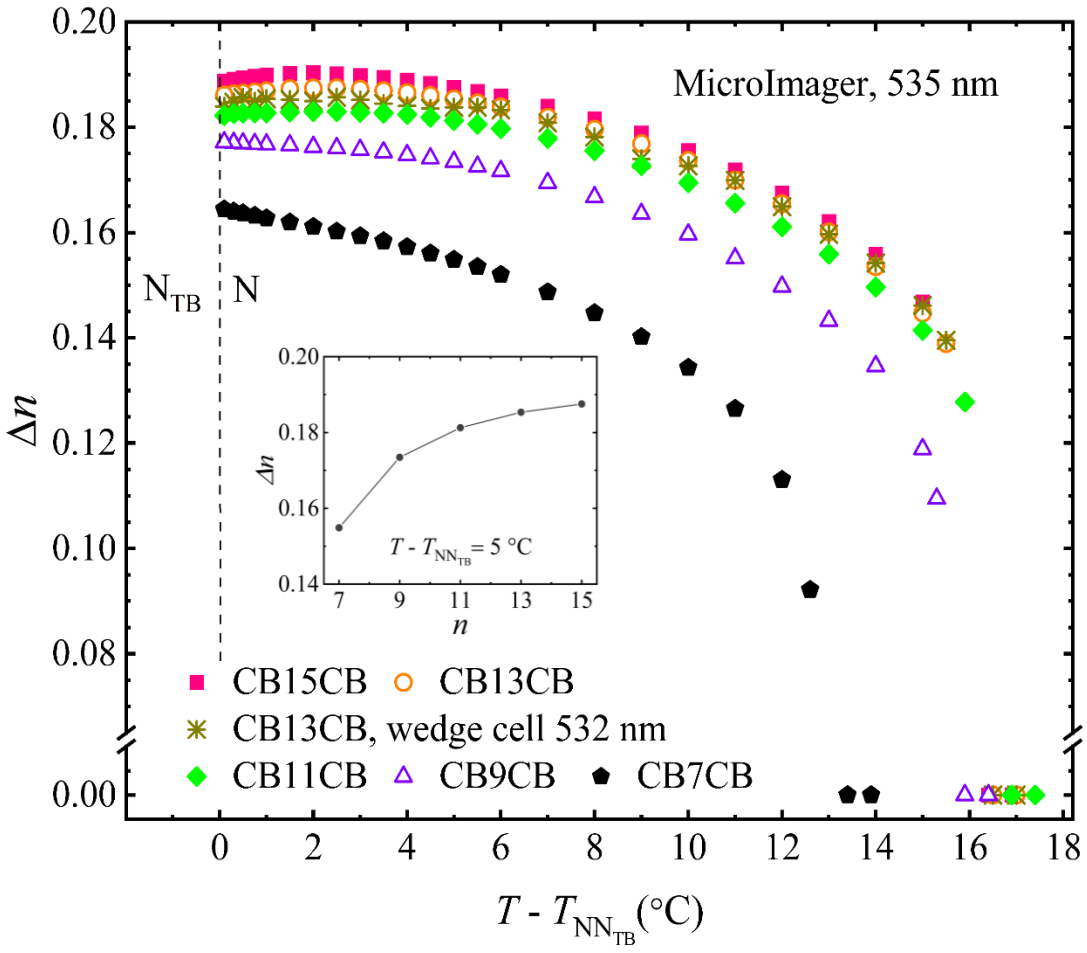

Figure 14. Temperature dependence of $\Delta n(T)$ for odd members of the CBnCB series in the N phase measured at the wavelength 535 nm. The inset shows the dependence on the molecular length at a fixed temperature $T - T_{\mathrm{NN_{TB}}} = 5$°C. The error bars are smaller than the size of the plot symbols.

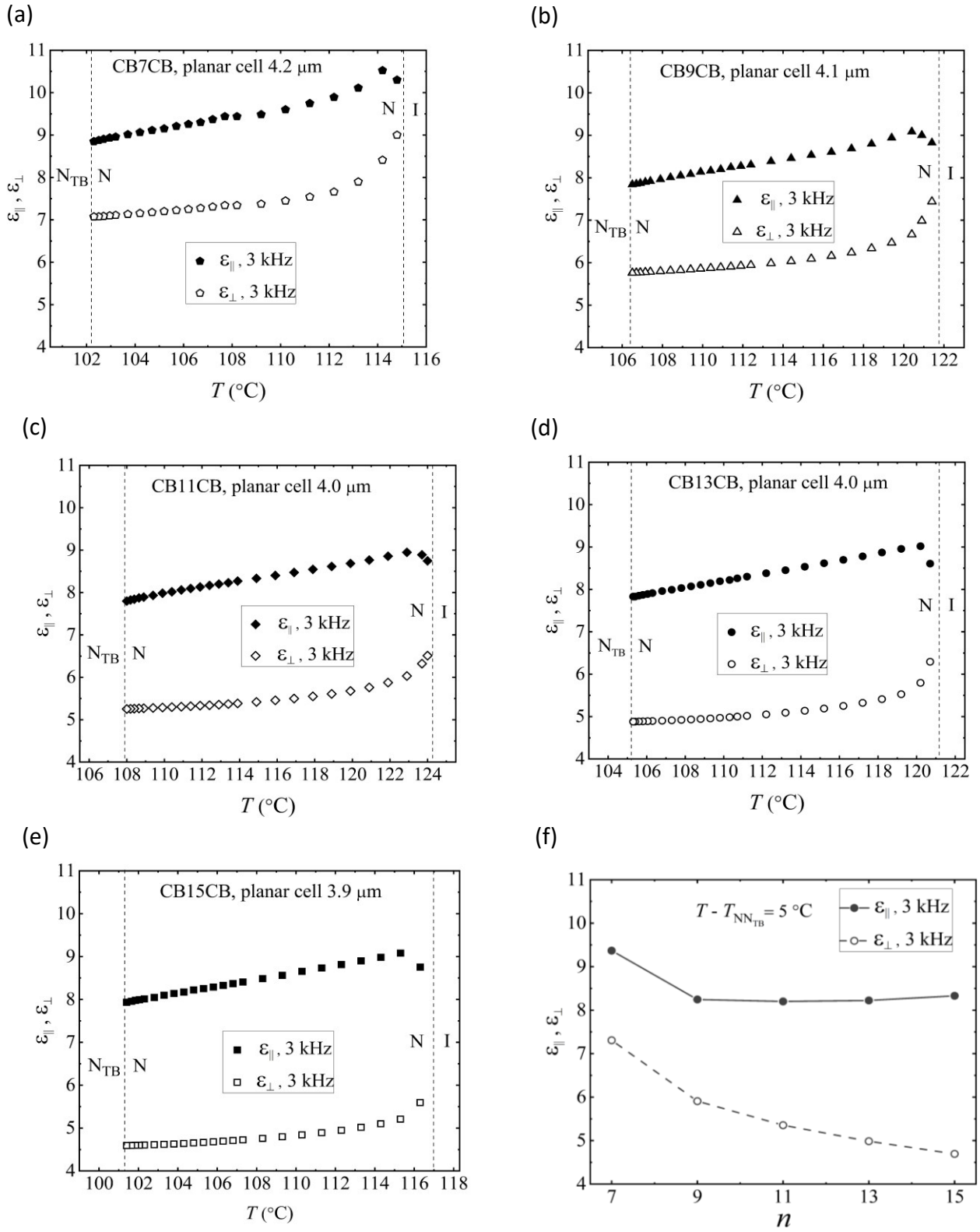

Figure 15. (a-e) Temperature dependencies of dielectric permittivities of the nematic phase at 3 kHz for (a) CB7CB, (b) CB9CB, (c) CB11CB, (d) CB13CB, and (e) CB15CB. (f) Dielectric permittivities as a function of the flexible spacer length n at a fixed temperature $T - T_{\mathrm{NN_{TB}}} = 5°\mathrm{C}$.

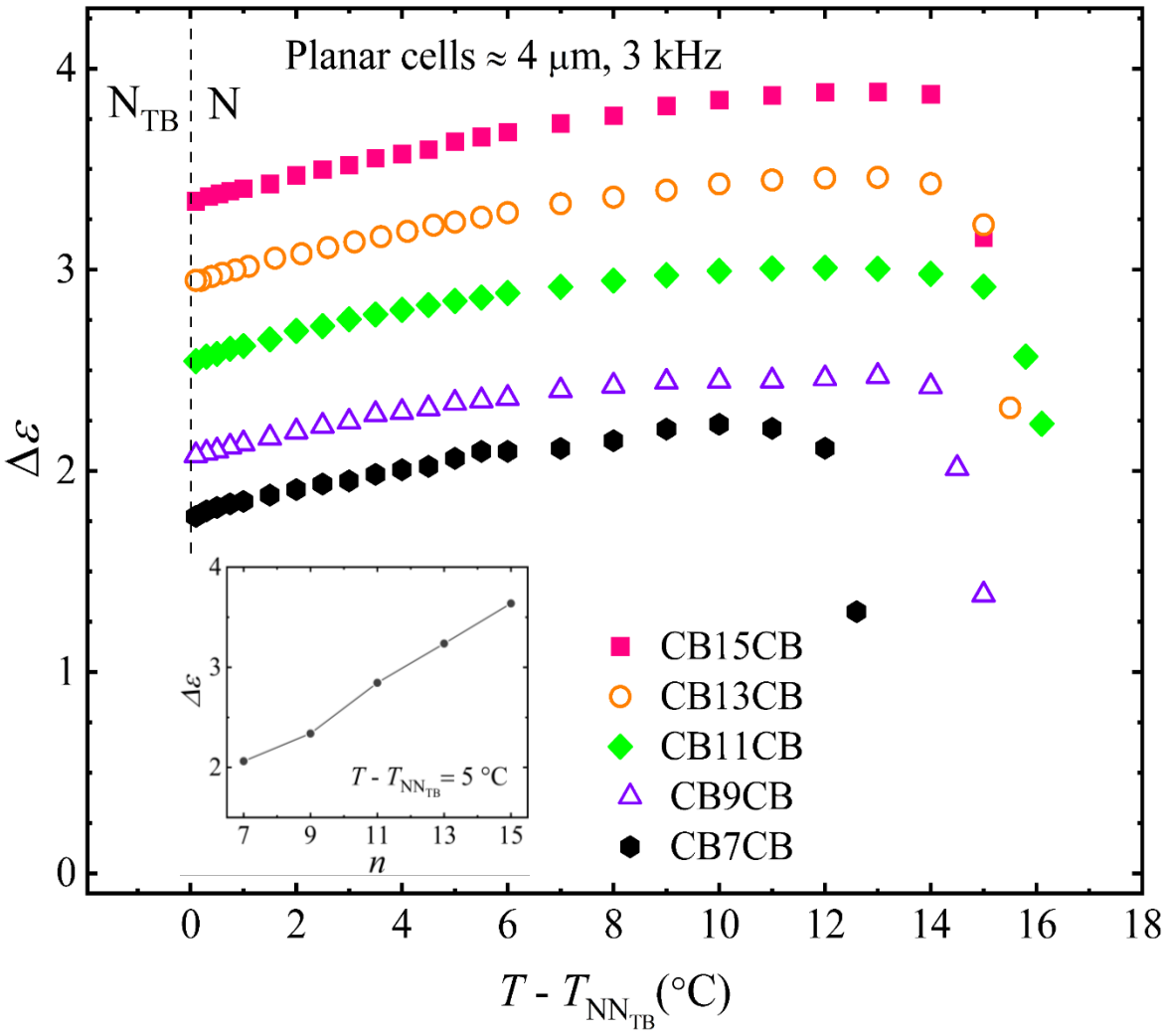

Figure 16. Temperature dependencies of dielectric anisotropy $\Delta\varepsilon(T)$ for CB*n*CB dimers in the nematic phase at 3 kHz; the inset shows the variation of $\Delta\varepsilon$ with flexible spacer length *n* at a fixed temperature $T - T_{\mathrm{NN_{TB}}} = 5°\mathrm{C}$.

3.4 Bend elastic constant, K_{33}, in the N^* phase

The transition temperatures of the CB*n*CB dimers and their binary chiral mixtures with S811 are shown in Table 2. These temperatures have been measured on cooling and this accounts for the small differences observed in the transition temperatures for CB15CB compared to those listed in Table 1. The textures of the chiral mixture CB13CB:S811 in the cholesteric (N*) and chiral twist bend nematic phase (N_{TB}*) are shown in Figure 17.

Table 2. Transition temperatures of the CB*n*CB dimers and the CB*n*CB: S811 (96:4 wt.%) chiral mixtures measured on cooling from the isotropic phase.

Compound	T_{IN} / ˚C	$T_{NN_{TB}}$ / ˚C	Chiral mixture	T_{IN^*} / ˚C	$T_{N^*N_{TB}^*}$ / ˚C
CB7CB	115.1	102.2	CB7CB:S811	107.0	94.1
CB9CB	121.8	106.4	CB9CB:S811	111.7	96.3
CB11CB	124.3	107.9	CB11CB:S811	116.5	100.3
CB13CB	121.2	105.2	CB13CB:S811	114.3	98.3
CB15CB	117.2	101.3	CB15CB:S811	113.7	97.8

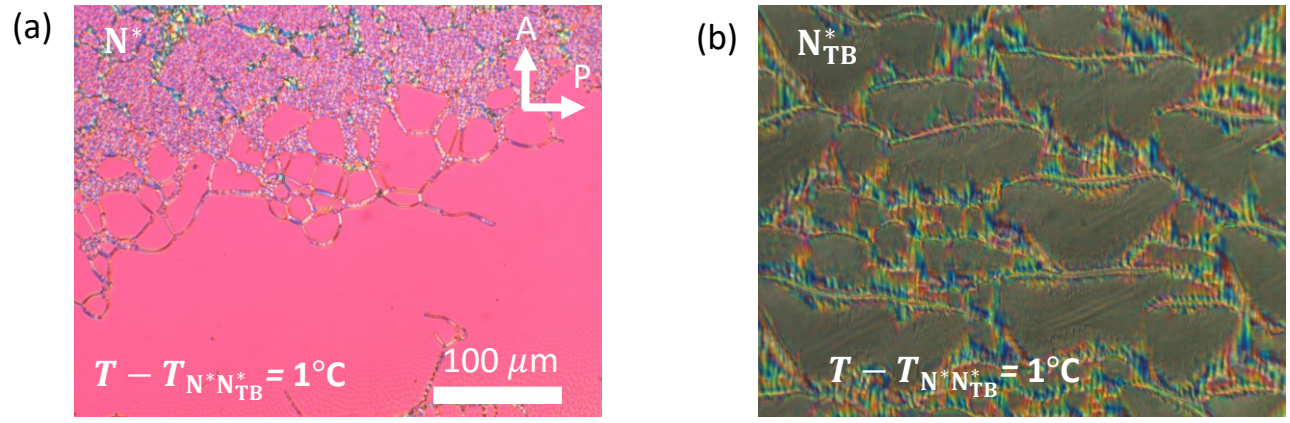

Figure 17. Optical textures of CB13CB:S811 in a 20 µm planar cell showing (a) the N^* phase and (b) the N_{TB}^* phase, the chiral analogue of the N_{TB} phase.

The measurement of K_{33} in the Ch_{OH} state is based on the dependence of the peak Bragg reflection wavelength $\boldsymbol{\lambda}_p$ on the applied electric field E [64, 77]. In this method, the experimentally measured $\boldsymbol{\lambda}_p/n_o(\boldsymbol{\lambda}_p)$ is plotted against E^{-1} at each temperature point of interest. The dispersion of the ordinary refractive index $n_o(\boldsymbol{\lambda}_p)$ is calculated using the Cauchy relation $n_o(\boldsymbol{\lambda}) = A + B\boldsymbol{\lambda}^{-2} + C\boldsymbol{\lambda}^{-4}$, where the coefficients A, B, and C are determined using n_o values measured at three different wavelengths, Figure 13. The plot of $\boldsymbol{\lambda}_p/n_o(\boldsymbol{\lambda}_p)$ against E^{-1} is fitted with the polynomial $\boldsymbol{\alpha}_1E^{-1} + \boldsymbol{\alpha}_2E^{-2}$ to find the fitting parameters $\boldsymbol{\alpha}_1$ and $\boldsymbol{\alpha}_2$, where the correction $\boldsymbol{\alpha}_2E^{-2}$ turns out to be negligibly small compared to $\boldsymbol{\alpha}_1E^{-1}$. The obtained value of $\boldsymbol{\alpha}_1$ is used to evaluate $K_{33} = \varepsilon_o\Delta\varepsilon(\alpha_1)^2/4\pi^2$. The dielectric anisotropy $\Delta\varepsilon(T)$ at the temperatures of interest is measured in the N phase of the corresponding chiral mixtures as described earlier.

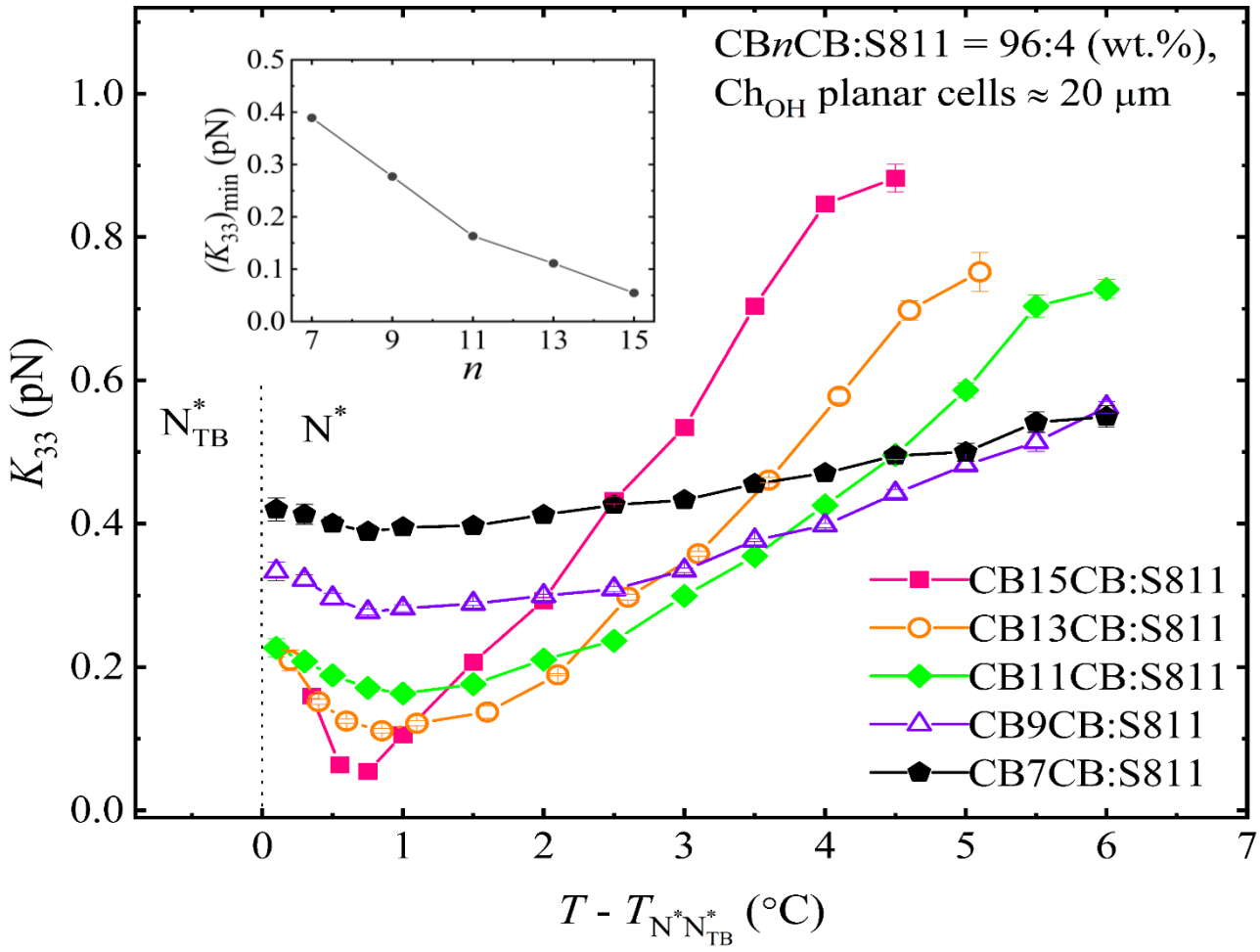

Figure 18. Temperature dependencies of the bend elastic constants $K_{33}(T)$ for the CB*n*CB:S811 chiral mixtures in the Ch_{OH} state. The inset shows the decrease of the minimum value of $K_{33}(T)$ with the flexible spacer length n. The reference transition temperatures are $T_{N^*N_{TB}^*}$ = 97.8˚C for n = 15, $T_{N^*N_{TB}^*}$ = 98.3˚C for n = 13, $T_{N^*N_{TB}^*}$ = 100.3˚C for n = 11, $T_{N^*N_{TB}^*}$ = 96.3˚C for n = 9, and $T_{N^*N_{TB}^*}$ = 94.1˚C for n = 7.

The measured temperature dependence $K_{33}(T)$ is non-monotonous in all CB*n*CB:S811 (96:4 wt.%) chiral mixtures, Figure 18. $K_{33}(T)$ decreases essentially linearly on cooling the N phase, passes through a minimum value at approximately T-$T_{N^*N_{TB}^*}$ = 1℃ and subsequently increases near the transition to the N_{TB}* phase. Similar behaviour has been reported for other odd-membered dimers [102]. This behaviour becomes more pronounced in higher homologues. For CB7CB:S811(96:4 wt.%), $K_{33}(T)$ in Figure 18 is very close to $K_{33}(T)$ reported previously for the N phase of pure CB7CB [73], and for the same CB7CB:S811 (96:4 wt.%) chiral mixture in the Ch_{OH} state [64]. Furthermore, $K_{33}(T)$ of the CB11CB:S811(96:4 wt.%) is similar to the data for a CB11CB:S811 (97:3 wt.%) mixture [64]. The minimum of $K_{33}(T)$

becomes deeper as n increases from 7 to 15, which reflects the higher flexibility of longer spacers, see inset in Figure 18. The lowest value of K_{33} = 0.05 pN in n = 15, is slightly smaller than the measured 0.065 pN in chiral mixtures CB7CB:CB11CB:5CB = 52:31:17 (wt.%) with 1.8 wt.% and 4.2 wt.% of S811 [64]. We note that the reflection spectra are hard to detect in the vicinity of the N*-N_{TB}* transition; in the CB7CB:S811, CB9CB:S811 and CB11CB:S811 mixtures, the reflection spectra are observed at $T \geq T_{N^*N_{TB^*}}$+0.1 ˚C; in CB13CB:S811, at $T \geq T_{N^*N_{TB^*}}$+0.2 ˚C, and in CB15CB:S811, at $T \geq T_{N^*N_{TB^*}}$+0.35 ˚C. The disappearance of the Bragg reflection in the pretransitional region may be associated with the destruction of the Ch_{OH} state by pretransitional cybotactic groups of the N_{TB}* phase; the equidistance of the pseudolayers of the N_{TB^*} clusters yields a higher value of K_{33} and prohibits the formation of the Ch_{OH} phase.

3.4 Molecular shape

We have already noted that it is widely accepted that the twist-bend nematic–nematic/isotropic transitions are predominantly shape driven. Indeed, a generalised Maier-Saupe molecular field theory developed to describe the phase behaviour of rigid V-shaped molecules revealed how sensitive the phase behaviour of such a system is to the molecular bend angle [103]. Specifically, as the bend angle becomes smaller, the temperature range of nematic behaviour is reduced and the N_{TB} phase becomes stabilised, and for bend angles ≤ 130° an N_{TB}-I transition is predicted. By contrast, for bend angles ≥ 150 °, the N_{TB}-N transition temperature is predicted to occur only at very low temperatures. Thus, to understand the dependence of the phase transition temperatures on the spacer length, n, shown in Figure 11, we must first consider how increasing n changes the molecular shape. Figure 19 compares the molecular shapes of the all-*trans* conformations of short, intermediate, and long members of the CBnCB series. CB1CB has a rather different shape and flexibility to the other members of the series and may described by a molecular bend angle of 116.0° defined by the C_{Ar}-C-C_{Ar} bond angle at the centre of the molecule. The question now arises as to how to best capture the difference in molecular shape as n increases. The most common approach to describe the bend of an odd-membered dimer is to use the angle subtended by the two nitrile bonds, given as angle Y in Figure 20, but this does not, in fact, differentiate between spacer lengths. Instead, the angle remains constant at approximately 113°, but the intersection of the lines falls progressively below the molecule as n increases, see Figure 20. It is quite apparent that the shapes of these molecules ($n \geq 3$) may be described as isosceles trapezoids, and a possible means of capturing the molecular bend of such a structure is to use the angle Z shown in Figure

20. The calculation of this angle is described in the ESI, and the values of this angle for the CB*n*CB series are listed in Table 3. It is clear that the molecular bend angle defined in this way increases as *n* increases, and it may, at first sight, appear counter-intuitive that the stability of the N_{TB} phase increases sharply as the bend angle increases over the first three members, see Figure 11. We must remember, however, that the flexibility of the molecule also increases on increasing *n*, and this facilitates the better interaction between the mesogenic groups. These interactions compensate for the loss of entropy due to the additional polar order in the N_{TB} phase [103], counteracting the effect of the increasing bend angle, and the stability of the N_{TB} phase increases. These interactions between the mesogenic units will also promote the emergence of the N phase. Thus, on increasing *n* we see initially an increase in the stability of both the N_{TB} and N phases. At some point the N phase will become more stable, and for the CB*n*CB series, this occurs for *n* =5. Further increasing *n* will continue to promote both the N and N_{TB} phases through the enhanced interactions between the mesogenic units whereas the increasing bend angle presumably destabilises the N_{TB} phase. Increasing *n* still further, dilutes the interactions between the mesogenic units as the volume fraction of alkyl chain increases, and both T_{NI} and $T_{N_{TB}N}$ would be expected to pass through maximum values and begin to decrease. For the CB*n*CB series this occurs for *n* = 11. As we have seen, however, the minimum value of $K_{33}(T)$ decreases monotonically on increasing spacer length reflecting the increased flexibility and this will drive the elastic instability related to the formation of the N_{TB} phase counteracting, at least in part, the expected decrease in $T_{N_{TB}N}$ related to the dilution of the mesogenic units. This interpretation accounts for the behaviour seen in Figure 11. We do note, however, that this is a simplified view of shape which has not taken into account the inherent flexibility of the spacer and a more realistic interpretation would necessarily consider a conformational distribution. Indeed, the very similar transition temperatures for the longer homologues presumably implies that their average molecular shapes are very similar.

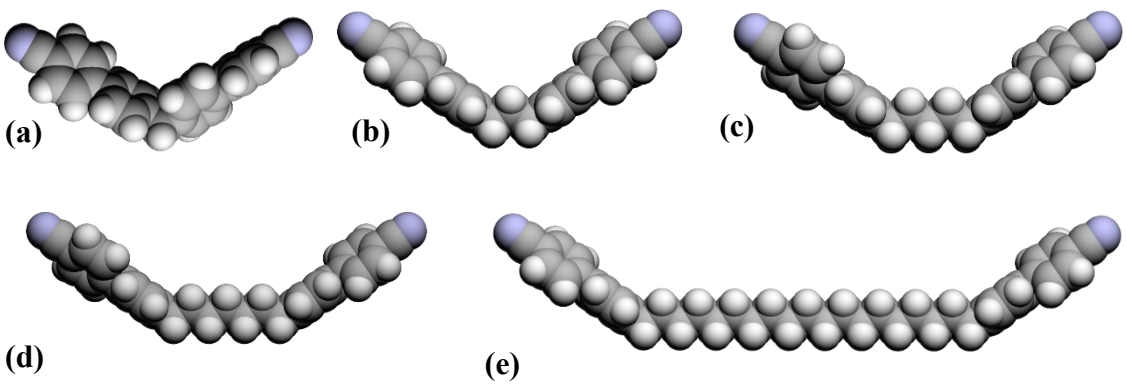

Figure 19. Space filling models comparing the all-*trans* molecular shapes of (a) CB1CB, (b) CB3CB, (c) CB5CB, (d) CB7CB and (e) CB19CB.

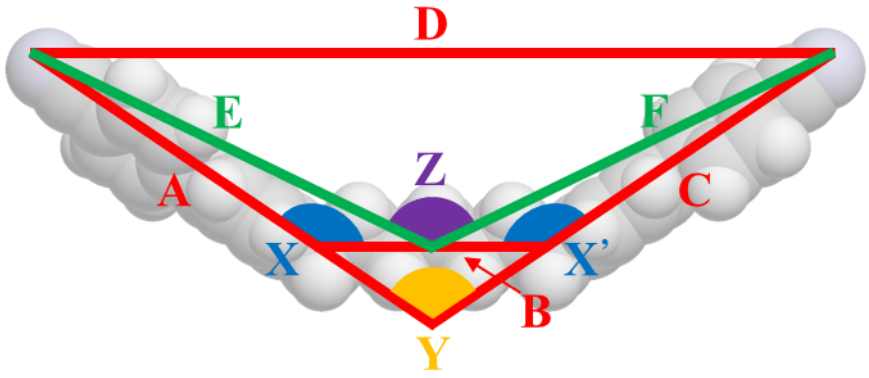

Figure 20. A spacer filling model of CB7CB showing the angle subtended by the two nitrile bonds falls below the molecule, *Y*, and the bend angle defined assuming the molecular shape is an isosceles trapezoid, *Z*.

Table 3 Molecular bend angles for the CB*n*CB and CBO*n*OCB series as defined in Figure 20.

CB*n*CB	Bend angle / °	CBO*n*OCB	Bend angle / °
1	116.0‡	-	-
3	117.6	1	144.8
5	123.0	3	150.3
7	127.9	5	152.7
9	131.9	7	154.5
11	135.3	9	156.0
13	138.3	11	157.3
15	140.9	-	-
17	143.1	-	-
19	145.1	-	-

‡The C_{Ar}-C-C_{Ar} bond angle.

3.5 CBOnOCB series

In order to investigate the effect of the bond angle, associated with the linking unit between the spacer and mesogenic units, on the transitional properties of the dimers, we revisited the CBO*n*OCB series, and established values of $T_{N_{TB}N}$ for n = 1, 7, 9, and 11, see Table 4. These complement our previous report of the values for 3 and 5 [67]. For n = 7, 9, and 11, the N_{TB} phase was identified on the basis of the observation of characteristic optical textures in isolated droplets when viewed under the polarised light microscope. These observations required extensive supercooling but the measured values are in excellent agreement with those reported recently by Arakawa and colleagues [34]. For CBO1OCB, the measured value of T_{NI} listed in Table 4 is somewhat higher than that reported previously whereas those for n = 7, 9, and 11 show excellent agreement [71, 72]. In order to estimate a virtual value of $T_{N_{TB}N}$ for CBO1OCB, a phase diagram was constructed for binary mixtures of CBO1OCB and CB7CB, see Figure 21. Mixtures containing ≥ 80 mol % CB7CB exhibited N_{TB} and N phases. The N-I transition temperatures showed a linear dependence on the concentration of CBO1OCB, and the experimentally measured value of T_{NI} for isolated droplets of CBO1OCB fell exactly on this line confirming the assignment. The N_{TB}-N line also showed a linear dependence on

concentration and extrapolation gave a virtual $T_{N_{TB}N}$ of 33°C. We note, however, that this estimate required a long extrapolation of the N_{TB}-N line and so the value obtained must treated with some degree of caution. Full details of these measurements are provided in the Supplementary Information along with representative textures from the mixtures as shown in Figure SI2.

Table 4. Transition temperatures and associated entropy changes for selected odd members of the CBO*n*OCB series.

n	T_{Cr-}/ °C	$T_{N_{TB}N}$/ °C	T_{NI}/ °C	$\Delta S_{Cr-}/R$	$\Delta S_{NI}/R$
1	149	33[a]	104[b]	10.8	-
7	138	85[b]	181	17.3	0.83
9	135	81[b]	172	14.7	1.03
11	125	78[b]	164	12.9	1.04

[a]Virtual transition temperature estimated from binary phase diagram with CB7CB. [b]Measured using the polarised light microscope.

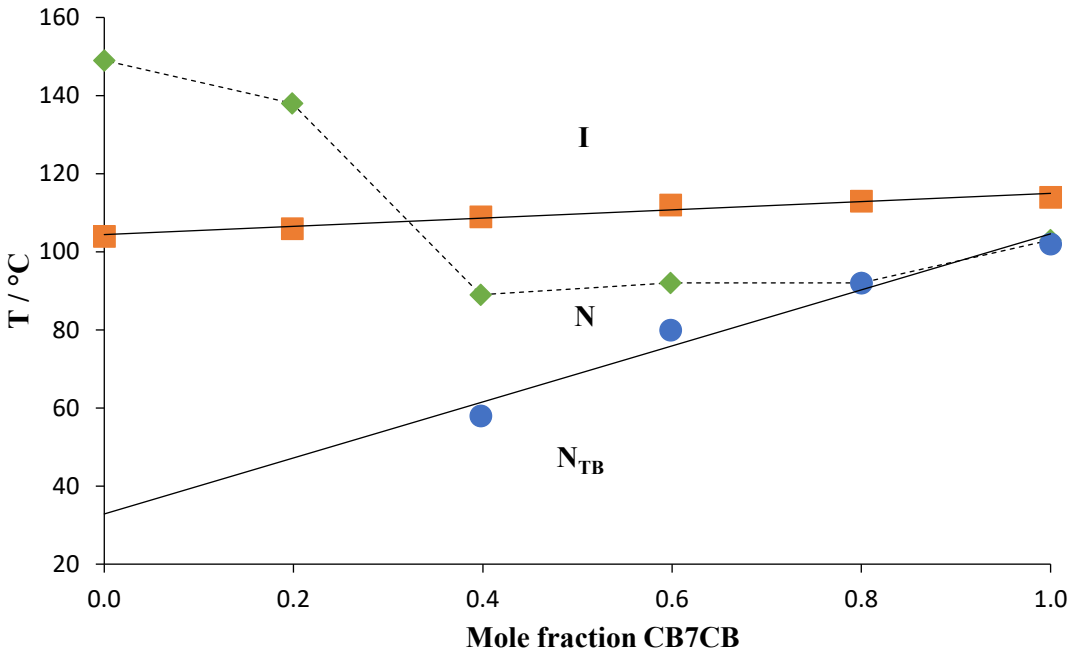

Figure 21. Phase diagram constructed for binary mixtures of CBO1OCB and CB7CB. Squares denote T_{NI}, circles $T_{N_{TB}N}$ and diamonds the melting points.

3.6 A comparison of the CBnCB and CBOnOCB series

The transition temperatures of the CB*n*CB and CBO*n*OCB series are compared in Figure 22. To make this a meaningful comparison, members of the two series having the same number of atoms connecting the two cyanobiphenyl units must be compared, and so the temperatures are plotted against *p*, where *p*=*n* for the CB*n*CB series and *n*+2 for the CBO*n*OCB series. The values of T_{NI} for the even members of both series decrease as *p* increases, and those of CBO*n*OCB series are higher by, on average, 24 K. By contrast, the values of T_{NI} for the odd members of both series initially increase on increasing *p*, pass through a weak maximum and subsequently gradually decrease. The values of T_{NI} are again higher for the CBO*n*OCB series, and for the odd members, this difference between the two series is greater. For example, T_{NI} for CBO5OCB is some 73 K higher than that of CB7CB. As *p* increases, this difference in T_{NI} becomes smaller and reaches a limiting value of around 32 K. The combined effect of these trends is that the values of T_{NI} show a large odd-even effect for both series in which the even members show the higher values, and the magnitude of the alternation is greater for the CB*n*CB series. Similar experimental observations have been made when comparing other methylene- and ether-linked dimers [104, 105], and these are in complete agreement with predictions of a theoretical model developed by Luckhurst and co-workers [106-108]. In this model the only difference between the dimers is their shape, and this difference arises from the bond angle between the *para* axis of the mesogenic unit and the first bond in the spacer. For an ether link this bond angle is 126.4° and for a methylene link it is considerably smaller, 113.5°. For an even-membered dimer, this difference in angle does not change the angle subtended by the major axes of the two mesogenic units but does increase the molecular breadth giving rise to a reduction in T_{NI}, see Figure 23. By comparison, the smaller bond angle associated with the methylene link means that an odd-membered methylene-linked dimer is significantly more bent than its even-membered counterpart and this leads to a larger reduction in T_{NI}, see Figure 23. The overall effect, therefore, is the values of T_{NI} for the methylene-linked dimer series show a more pronounced alternation than those of the corresponding ether-linked series. In addition, it is important to note that these alternations in T_{NI} attenuate on increasing *p* for both series such that for the longer spacers, odd and even membered dimers show essentially the same value of T_{NI}. This attenuation may be accounted for in terms of the increasing number of conformations available to the spacer and torsional fluctuations which results in a loss of orientational correlations between the mesogenic units. In addition to these shape-based arguments, we should also note that the strength of the interactions between cyanobiphenyloxy

units will be greater than those between the cyanobiphenyl units, and this contributes to the higher values of T_{NI} seen for both the odd and even members of the CBO*n*OCB series.

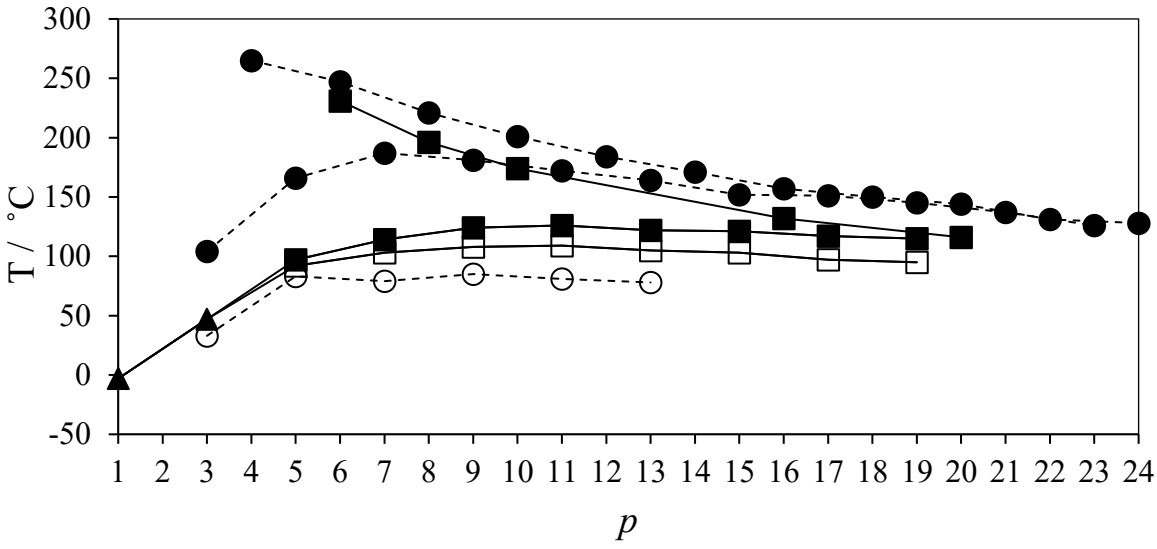

Figure 22. The dependence of the transition temperatures on the number of atoms, *p*, connecting the mesogenic units in the CB*n*CB and CBO*n*OCB series; for the CB*n*CB series *p*=*n*, and for the CBO*n*OCB series, *p*=*n*+*2*. Filled circles represent N-I and open circles N_{TB}-N transitions for the CBO*n*OCB series. Filled squares represent N-I, open squares N_{TB}-N transitions, and filled triangles N_{TB}-I transitions for the CB*n*CB series. Solid lines connect data points for the CB*n*CB series and the broken lines for the CBO*n*OCB series. The data have been taken from a number of sources [67, 71, 72]. The transition temperatures of the CBO*n*OCB series ($n \geq 13$) were reported prior to the discovery of the N_{TB} phase and these have not been revisited [71].

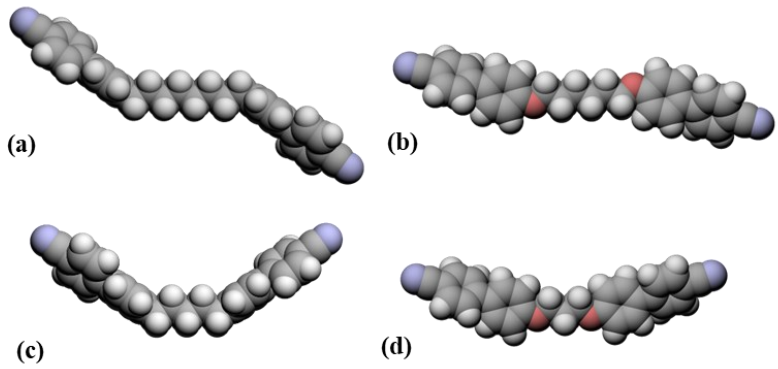

Figure 23. Space filling models comparing the all-*trans* molecular shapes of (a) CB6CB, (b) CBO4OCB, (c) CB5CB, and (d) CBO3OCB, highlighting the effect of changing the linking unit between the spacer and mesogenic units.

We now turn our attention to the tendency of these two series to exhibit the N_{TB} phase. We have seen that CB1CB exhibits a virtual N_{TB}-I transition at –3˚C whereas for CB3CB the N_{TB}-I transition is experimentally observed at 47 °C. By comparison, for CBO1OCB a virtual value of $T_{N_{TB}N}$ was estimated at 33 °C, and experimentally T_{NI} observed at 104 °C. Presumably this difference in behaviour reflects the more bent shape of CB3CB arising from the methylene links, see Figure 19, and the greater ability of the mesogenic units in CBO1OCB to interact. Over the shortest odd members, the values of $T_{N_{TB}I}$ or $T_{N_{TB}N}$ increase sharply. For p=5, the value of $T_{N_{TB}N}$ for CB5CB is 9 K higher than that of CBO3OCB, although T_{NI} for the latter is 69 K higher than that of CB5CB. After p=5, the dependence of $T_{N_{TB}N}$ on p for both series becomes rather weak, and the values of $T_{N_{TB}N}$ for the CB*n*CB series are on average 25 K higher. By contrast a stronger dependence is observed for the values of T_{NI} which increase by 8 K between p = 7 and 13 for the CB*n*CB series but decrease for the CBO*n*OCB series by 31 K. As noted earlier, increasing the spacer length in these odd-membered dimers increases the ability of the mesogenic units to interact but also dilutes these interactions. For the N-I transition, the latter effect appears to dominate for the CBO*n*OCB series and the former for the CB*n*CB series reflecting the more bent shape of the methylene-linked dimers, see Table 3. The less sensitive nature of $T_{N_{TB}N}$ on p presumably reflects its stronger dependence on shape and hence, as discussed earlier, on K_{33}. For the odd-membered dimers with p = 7-13, the CB*n*CB series shows a larger change in the bend angle but presumably this is offset by the greater ability of the mesogenic units to interact as the bend angle increases giving little overall change in the value of $T_{N_{TB}N}$ as spacer length increases.

3.7 CB16CB and CB20CB

The transitional properties of the two new long even-members of the CB*n*CB series, CB16CB and CB20CB, are also listed in Table 1. Both dimers exhibit enantiotropic nematic behaviour and no other liquid crystalline phase. As described earlier, the values of T_{NI} for the even members of the CB*n*CB series decrease on increasing *n,* whereas those of the odd members initially increase with *n*, pass through a maximum and tend towards a limiting value, Figure 22. The value of T_{NI} for CB20CB is essentially the same as that of the adjacent odd members suggesting that their average molecular shapes are similar. Figure 24 shows the all-*trans* molecular shapes for CB16CB and CB17CB. In the even-membered dimer the mesogenic units are parallel whereas the odd member adopts the trapezium shape discussed earlier. Presumably the conformational flexibility of these long spacers allows the mesogenic units in the odd and even members to interact to much the same extent and may suggest that their average molecular shapes are similar. This begs the fascinating question, can long even-membered dimers exhibit the N_{TB} phase? To explore this intriguing possibility, phase diagrams were constructed for binary mixtures of each dimer with CB7CB, see Figure 25. In both phase diagrams, T_{NI} varies in a linear fashion with composition as might be expected given their very similar molecular structures. Increasing the concentration of the even-membered dimer in the mixture sees the value of $T_{N_{TB}N}$ fall rapidly, and the N_{TB} phase is not observed in either system for mixtures containing ≤ 70 mol % CB7CB. The virtual value of $T_{N_{TB}N}$ for the even membered dimers may be estimated by extrapolation of the $T_{N_{TB}N}$ line although it is stressed that the extrapolation is rather long in both cases. The estimated values of $T_{N_{TB}N}$ for CB16CB and CB20CB are -13 °C and 1°C, respectively, and around 100 K lower than seen for the adjacent odd members. This strongly suggests that, on average, the long odd-membered dimers are more bent than their even-membered counterparts, and the similarity in their values of T_{NI} may be attributed to the increased ease at which the mesogenic units in odd-membered dimers can interact on increasing the spacer length.

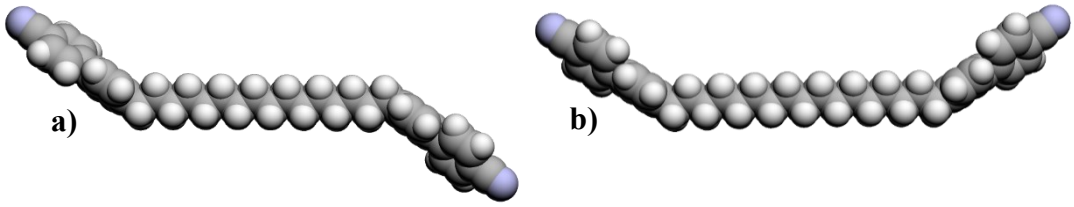

Figure 24. Space filling models comparing the all-*trans* molecular shapes of (a) CB16CB, and (b) CB17CB.

(a)

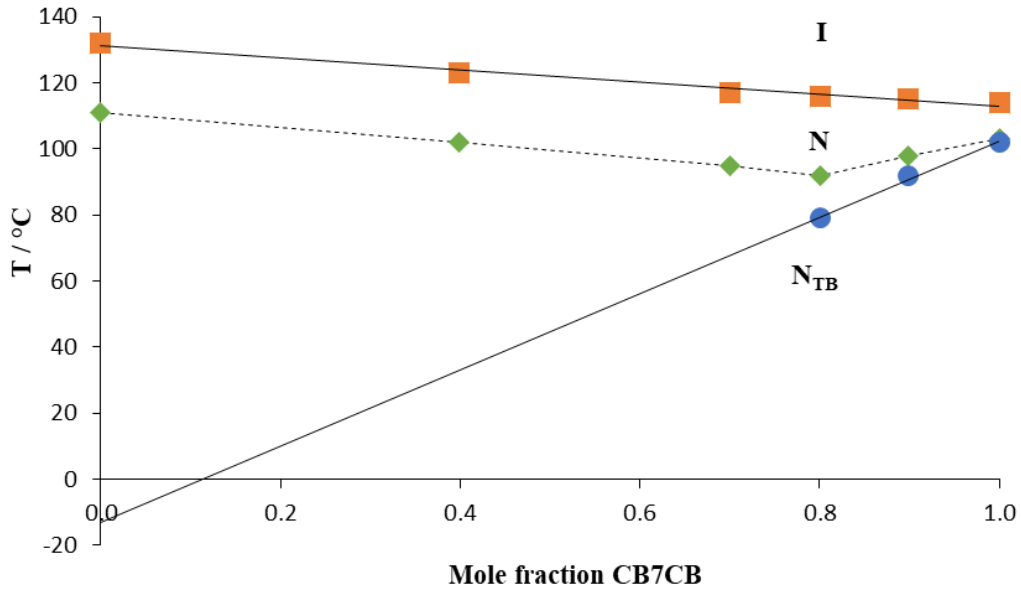

(b)

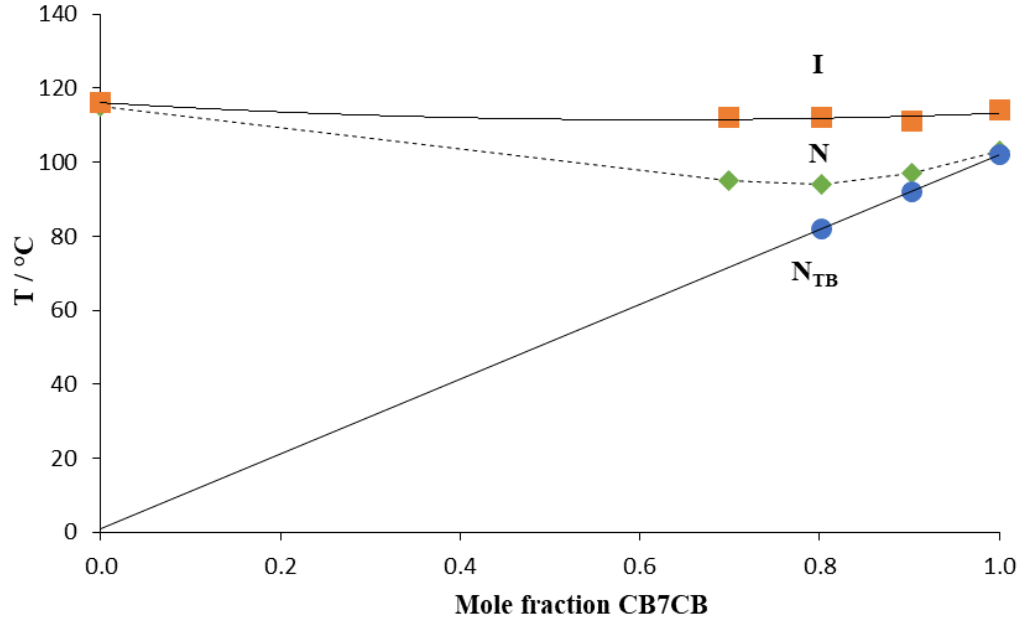

Figure 25. Phase diagrams constructed using binary mixtures of (a) CB16CB and CB7CB, and (b) CB20CB and CB7CB. The squares indicate N-I transitions, the circles N_{TB}-N transitions and the diamonds melting points. The solid lines indicate the T_{NI} and $T_{N_{TB}N}$ trends, and the dotted line connects the melting points.

4. Conclusions

We have reported the transitional properties of the CB*n*CB series, the most complete set of odd-membered dimers to date. This has revealed that the shortest members show direct N_{TB}-I transitions and as spacer length increases, we see the N_{TB}-N-I sequence. These observations and a comparison of the transitional properties of the CB*n*CB and CBO*n*OCB series have reinforced the importance of shape in the formation of the N_{TB} phase. This is attributed to the dependence of material properties such as dielectric permittivities, refractive indices, and bend elastic constant on molecular shape. A longer flexible spacer yields higher birefringence and dielectric anisotropy. The temperature dependence of the bend modulus is non-monotonous, with a pronounced minimum at about 1℃ above the transition point to the twist-bend phase; the minimum is deeper for longer homologues, with CB15CB doped with a chiral S811 showing the lowest bend elastic constant (0.05 pN) in any liquid crystal measured so far. In an attempt to capture the shape of these symmetric dimers we have suggested that they be approximated to an isosceles trapezium. This approach reveals a bend angle which increases as the spacer length increases, effectively resulting in longer and more linear molecular shapes. These shape changes might explain the increase of the birefringence and dielectric anisotropy with *n*, a behaviour clearly at odds with the previously reported dependencies on the length of aliphatic terminal chains in homologous series of cyanobiphenyls and similar nematic mesogens [96]. Although it is apparent that the N_{TB}-N phase transition is predominantly shape driven it is not entirely so. This is clear when comparing the values of $T_{N_{TB}N}$ for the CB*n*CB and CBO*n*OCB series. As would be expected, the values of T_{NI} for the CBO*n*OCB series are much higher than those of the corresponding members of the CB*n*CB series. By comparison, their values of $T_{N_{TB}N}$ are rather similar and this appears counter intuitive if considering shape alone. It is clear that the interaction strength between the mesogenic units also plays a role in determining $T_{N_{TB}N}$. Thus, although the odd members of the CB*n*CB series are clearly more bent than the corresponding CBO*n*OCB dimers, the stronger interactions between the cyanobiphenyloxy units ensures that the values of $T_{N_{TB}N}$ for the longer members of the series are surprisingly similar. These stronger interactions are manifested to a much greater extent in much higher values of T_{NI} for the CBO*n*OCB series. We have reported also that whereas long even-membered and odd-membered dimers show very similar values of T_{NI}, the former do not exhibit N_{TB} behaviour. This is attributed to the ability of the mesogenic units in these dimers to interact essentially the same irrespective of the parity of the spacer but the odd members retain their more bent shape. Thus, the transitional behaviour of dimers may be interpreted in

terms of the molecular bend angle, the ability of the mesogenic units to interact, and the diluting factor of the spacer chain.

Acknowledgements

The RSoXS experiments were performed at beamline 11.0.1.2 at the Advanced Light Source at the Lawrence Berkeley National Laboratory, supported by the Director of the Office of Science, Office of Basic Energy Sciences, of the U.S. Department of Energy under Contract No. DE-AC02- 05CH11231. ODL and KT research was supported by the US National Science Foundation grant DMR-2215191.

References

1. Cestari M, Diez-Berart S, Dunmur DA, Ferrarini A, de la Fuente MR, Jackson DJB, et al. Phase behavior and properties of the liquid-crystal dimer 1 '',7 ''-bis(4-cyanobiphenyl-4 '- yl) heptane: A twist-bend nematic liquid crystal. Phys Rev E. 2011;84:031704.
2. Borshch V, Kim YK, Xiang J, Gao M, Jakli A, Panov VP, et al. Nematic twist-bend phase with nanoscale modulation of molecular orientation. Nature Commun. 2013;4:2635.
3. Chen D, Porada JH, Hooper JB, Klittnick A, Shen Y, Tuchband MR, et al. Chiral heliconical ground state of nanoscale pitch in a nematic liquid crystal of achiral molecular dimers. Proc Natl Acad Sci U S A. 2013;110:15931-15936.
4. Meyer RB. Structural problems in liquid crystal physics, Les houches summer school in theoretical physics. In: Balian R, G W, editors. Molecular Fluids New York: Gordon and Breach; 1976. p. 273-373.
5. Dozov I. On the spontaneous symmetry breaking in the mesophases of achiral banana-shaped molecules. Europhys Lett. 2001;56:247-253.
6. Henderson PA, Imrie CT. Methylene-linked liquid crystal dimers and the twist-bend nematic phase. Liq Cryst. 2011;38:1407-1414.
7. Dawood AA, Grossel MC, Luckhurst GR, Richardson RM, Timimi BA, Wells NJ, et al. Twist-bend nematics, liquid crystal dimers, structure-property relations. Liq Cryst. 2017;44:106-126.
8. Dawood AA, Grossel MC, Luckhurst GR, Richardson RM, Timimi BA, Wells NJ, et al. On the twist-bend nematic phase formed directly from the isotropic phase. Liq Cryst. 2016;43:2-12.
9. Lesac A, Baumeister U, Dokli I, Hamersak Z, Ivsic T, Kontrec D, et al. Geometric aspects influencing N-N-TB transition - implication of intramolecular torsion. Liq Cryst. 2018;45:1101-1110.
10. Knezevic A, Dokli I, Novak J, Kontrec D, Lesac A. Fluorinated twist-bend nematogens: the role of intermolecular interaction. Liq Cryst. 2021;48:756-766.
11. Panov VP, Vij JK, Mehl GH. Twist-bend nematic phase in cyanobiphenyls and difluoroterphenyls bimesogens. Liq Cryst. 2017;44:147-159.
12. Arakawa Y, Ishida Y, Komatsu K, Arai Y, Tsuji H. Thioether-linked benzylideneaniline-based twist-bend nematic liquid crystal dimers: Insights into spacer lengths, mesogenic arm structures, and linkage types. Tetrahedron. 2021;95:132351.

13. Arakawa Y, Komatsu K, Shiba T, Tsuji H. Methylene- and thioether-linked cyanobiphenyl-based liquid crystal dimers CBnSCB exhibiting room temperature twist-bend nematic phases and glasses. Mater Adv. 2021;2:1760-1773.
14. Arakawa Y, Komatsu K, Ishida Y, Igawa K, Tsuji H. Carbonyl- and thioether-linked cyanobiphenyl-based liquid crystal dimers exhibiting twist-bend nematic phases. Tetrahedron. 2021;81:131870.
15. Arakawa Y, Komatsu K, Ishida Y, Tsuji H. Thioether-linked azobenzene-based liquid crystal dimers exhibiting the twist-bend nematic phase over a wide temperature range. Liq Cryst. 2021;48:641-652.
16. Mandle RJ. A Ten-Year Perspective on Twist-Bend Nematic Materials. Molecules. 2022;27:2689.
17. Archbold CT, Andrews JL, Mandle RJ, Cowling SJ, Goodby JW. Effect of the linking unit on the twist-bend nematic phase in liquid crystal dimers: a comparative study of two homologous series of methylene- and ether-linked dimers. Liq Cryst. 2017;44:84-92.
18. Mandle RJ. Designing Liquid-Crystalline Oligomers to Exhibit Twist-Bend Modulated Nematic Phases. Chem Rec. 2018;18:1341-1349.
19. Paterson DA, Gao M, Kim YK, Jamali A, Finley KL, Robles-Hernandez B, et al. Understanding the twist-bend nematic phase: the characterisation of 1-(4-cyanobiphenyl-4 '-yloxy)-6-(4-cyanobiphenyl-4 '-yl)hexane (CB6OCB) and comparison with CB7CB. Soft Matter. 2016;12:6827-6840.
20. Paterson DA, Xiang J, Singh G, Walker R, Agra-Kooijman DM, Martinez-Felipe A, et al. Reversible Isothermal Twist-Bend Nematic-Nematic Phase Transition Driven by the Photoisomerization of an Azobenzene-Based Nonsymmetric Liquid Crystal Dinner. J Am Chem Soc. 2016;138:5283-5289.
21. Paterson DA, Walker R, Abberley JP, Forestier J, Harrison WTA, Storey JMD, et al. Azobenzene-based liquid crystal dimers and the twist-bend nematic phase. Liq Cryst. 2017;44:2060-2078.
22. Forsyth E, Paterson DA, Cruickshank E, Strachan GJ, Gorecka E, Walker R, et al. Liquid crystal dimers and the twist-bend nematic phase: On the role of spacers and terminal alkyl chains. J Molec Liq. 2020;320:114391.
23. Walker R, Majewska M, Pociecha D, Makal A, Storey JMD, Gorecka E, et al. Twist-Bend Nematic Glasses: The Synthesis and Characterisation of Pyrene-based Nonsymmetric Dimers. Chemphyschem. 2021;22:461-470.
24. Walker R, Pociecha D, Strachan GJ, Storey JMD, Gorecka E, Imrie CT. Molecular curvature, specific intermolecular interactions and the twist-bend nematic phase: the synthesis and characterisation of the 1-(4-cyanobiphenyl-4-yl)-6-(4-alkylanilinebenzylidene-4-oxy)hexanes (CB6O.m). Soft Matter. 2019;15:3188-3197.
25. Cruickshank E, Salamonczyk M, Pociecha D, Strachan GJ, Storey JMD, Wang C, et al. Sulfur-linked cyanobiphenyl-based liquid crystal dimers and the twist-bend nematic phase. Liq Cryst. 2019;46:1595-1609.
26. Cruickshank E, Walker R, Strachan GJ, Goode CHF, Majewska MM, Pociecha D, et al. The influence of the imine bond direction on the phase behaviour of symmetric and non-symmetric liquid crystal dimers. J Molec Liq. 2023;391:123226.
27. Abberley JP, Storey JMD, Imrie CT. Structure-property relationships in azobenzene-based twist-bend nematogens. Liq Cryst. 2019;46:2102-2114.

28. Majewska MM, Forsyth E, Pociecha D, Wang C, Storey JMD, Imrie CT, et al. Controlling spontaneous chirality in achiral materials: liquid crystal oligomers and the heliconical twist-bend nematic phase. Chem Commun. 2022;58:5285-5288.
29. Tuchband MR, Paterson DA, Salamonczykc M, Norman VA, Scarbrough AN, Forsyth E, et al. Distinct differences in the nanoscale behaviors of the twist-bend liquid crystal phase of a flexible linear trimer and homologous dimer. Proc Natl Acad Sci U S A. 2019;116:10698-10704.
30. Mandle RJ, Goodby JW. A Nanohelicoidal Nematic Liquid Crystal Formed by a Non-Linear Duplexed Hexamer. Angew Chem Int Ed. 2018;57:7096-7100.
31. Simpson FP, Mandle RJ, Moore JN, Goodby JW. Investigating the Cusp between the nano-and macro-sciences in supermolecular liquid-crystalline twist-bend nematogens. J Mater Chem C. 2017;5:5102-5110.
32. Al-Janabi A, Mandle RJ, Goodby JW. Isomeric trimesogens exhibiting modulated nematic mesophases. RSC Adv. 2017;7:47235-47242.
33. Arakawa Y, Komatsu K, Inui S, Tsuji H. Thioether-linked liquid crystal dimers and trimers: The twist-bend nematic phase. J Molec Str. 2020;1199:126913.
34. Arakawa Y, Komatsu K, Shiba T, Tsuji H. Phase behaviors of classic liquid crystal dimers and trimers: Alternate induction of smectic and twist-bend nematic phases depending on spacer parity for liquid crystal trimers. J Molec Liq. 2021;326:115319.
35. Arakawa Y, Komatsu K, Ishida Y, Shiba T, Tsuji H. Thioether-Linked Liquid Crystal Trimers: Odd-Even Effects of Spacers and the Influence of Thioether Bonds on Phase Behavior. Materials. 2022;15:1709.
36. Chen D, Nakata M, Shao RF, Tuchband MR, Shuai M, Baumeister U, et al. Twist-bend heliconical chiral nematic liquid crystal phase of an achiral rigid bent-core mesogen. Phys Rev E. 2014;89:022506.
37. Sreenilayam SP, Panov VP, Vij JK, Shanker G. The N-TB phase in an achiral asymmetrical bent-core liquid crystal terminated with symmetric alkyl chains. Liq Cryst. 2017;44:244-253.
38. Walker R, Pociecha D, Crawford CA, Storey JMD, Gorecka E, Imrie CT. Hydrogen bonding and the design of twist-bend nematogens. J Molec Liq. 2020;303:112630.
39. Walker R, Pociecha D, Martinez-Felipe A, Storey JMD, Gorecka E, Imrie CT. Twist-Bend Nematogenic Supramolecular Dimers and Trimers Formed by Hydrogen Bonding. Crystals. 2020;10:175.
40. Walker R, Pociecha D, Abberley JP, Martinez-Felipe A, Paterson DA, Forsyth E, et al. Spontaneous chirality through mixing achiral components: a twist-bend nematic phase driven by hydrogen-bonding between unlike components. Chem Commun. 2018;54:3383-3386.
41. Walker R. The twist-bend phases: structure-property relationships, chirality and hydrogen-bonding. Liq Cryst Today. 2020;29:2-14.
42. Jansze SM, Martinez-Felipe A, Storey JMD, Marcelis ATM, Imrie CT. A Twist-Bend Nematic Phase Driven by Hydrogen Bonding. Angew Chem Int Ed. 2015;54:643-646.
43. Stevenson WD, An JG, Zeng XB, Xue M, Zou HX, Liu YS, et al. Twist-bend nematic phase in biphenylethane-based copolyethers. Soft Matter. 2018;14:3003-3011.
44. Tufaha N, Gibb CJ, Storey JMD, Imrie CT. Can even-membered liquid crystal dimers exhibit the twist-bend nematic phase? The preparation and properties of disulphide and thioether linked dimers. Liq Cryst. 2023;50:1362-1374.
45. Archbold CT, Davis EJ, Mandle RJ, Cowling SJ, Goodby JW. Chiral dopants and the twist-bend nematic phase - induction of novel mesomorphic behaviour in an apolar bimesogen. Soft Matter. 2015;11:7547-7557.

46. Walker R, Pociecha D, Salamonczyk M, Storey JMD, Gorecka E, Imrie CT. Intrinsically Chiral Twist-Bend Nematogens: Interplay of Molecular and Structural Chirality in the N-TB Phase. Chemphyschem. 2023;24:e202300105.
47. Walker R, Pociecha D, Salamonczyk M, Storey JMD, Gorecka E, Imrie CT. Supramolecular liquid crystals exhibiting a chiral twist-bend nematic phase. Mater Adv. 2020;1:1622-1630.
48. Walker R, Pociecha D, Storey JMD, Gorecka E, Imrie CT. The Chiral Twist-Bend Nematic Phase (N*(TB)). Chem Eur J. 2019;25:13329-13335.
49. Imrie CT, Walker R, Storey JMD, Gorecka E, Pociecha D. Liquid Crystal Dimers and Smectic Phases from the Intercalated to the Twist-Bend. Crystals. 2022;12:1245.
50. Alshammari AF, Pociecha D, Walker R, Storey JMD, Gorecka E, Imrie CT. New patterns of twist-bend liquid crystal phase behaviour: the synthesis and characterisation of the 1-(4-cyanobiphenyl-4 '-yl)-10-(4-alkylaniline-benzylidene-4 '-oxy)decanes (CB10O center dot m). Soft Matter. 2022;18:4679-4688.
51. Pociecha D, Vaupotic N, Majewska M, Cruickshank E, Walker R, Storey JMD, et al. Photonic Bandgap in Achiral Liquid Crystals-A Twist on a Twist. Adv Mater. 2021;33:2103288.
52. Salamonczyk M, Vaupotic N, Pociecha D, Walker R, Storey JMD, Imrie CT, et al. Multi-level chirality in liquid crystals formed by achiral molecules. Nat Commun. 2019;10:1922.
53. Abberley JP, Killah R, Walker R, Storey JMD, Imrie CT, Salamonczyk M, et al. Heliconical smectic phases formed by achiral molecules. Nat Commun. 2018;9:228.
54. Cruickshank E, Anderson K, Storey JMD, Imrie CT, Gorecka E, Pociecha D, et al. Helical phases assembled from achiral molecules: Twist-bend nematic and helical filamentary B-4 phases formed by mesogenic dimers. J Molec Liq. 2022;346:118180.
55. Meyer C, Davidson P, Luckhurst GR, Dokli I, Knezevic A, Lesac A, et al. Temperature Dependence of the Electroclinic Effect in the Twist-Bend Nematic Phase. Crystals. 2023;13:465.
56. Sellares J, Diego JA, Lopez DO, Salud J, Robles-Hernandez B, de la Fuente MR, et al. Comparative dielectric and thermally stimulated-depolarization-current studies of the liquid crystal dimers 1 '',9 ''-bis(4-cyanobiphenyl-4 '-yl) nonane and heptane and a binary mixture between them, close to the glass transition. Phys Rev E. 2022;106:054702.
57. Oswald P, Poy G, Krishnamurthy KS. Structure and Lehmann rotation of drops in a surfactant-doped bent-core liquid crystal. Phys Rev E. 2022;106:024705.
58. Yu G, Wilson MR. All-atom simulations of bent liquid crystal dimers: the twist-bend nematic phase and insights into conformational chirality. Soft Matter. 2022;18:3087-3096.
59. Dunmur D. Anatomy of a Discovery: The Twist-Bend Nematic Phase. Crystals. 2022;12:309.
60. Ferrarini A, Greco C, Luckhurst GR, Timimi BA, Zimmermann H. Exploring the behaviour of the twist-bend nematic phase using NMR with a variety of spin probes. Liq Cryst. 2020;47:2074-2091.
61. Krishnamurthy KS, Rao DSS, Khatavi SY, Yelamaggad CV. Twist-bend nematic drops as colloidal particles: Electric instabilities. Phys Rev E. 2023;107:044703.
62. Imrie CT, Paterson DA, Storey JMD, Chamignon C, Lelli M, Emsley JW, et al. Phase transitions in a high magnetic field of an odd, symmetric liquid crystal dimer having two nematic phases, N-U and N-TB, studied by NMR spectroscopy. Phys Rev E. 2020;102:042706.
63. Luckhurst GR, Timimi BA, Wells NJ, Zimmermann H. On orientational order in nematic and twist-bend nematic phases: a H-2-NMR study of binary mixtures of the odd dimer,1 '',9

''-bis(4-cyanobiphenyl-4 '-yl) nonane, (CB9CB), and the monomer, 4-pentyl-4 '-cyanobiphenyl, (5CB-d(2)). Liq Cryst. 2018;45:1913-1928.
64. Iadlovska OS, Babakhanova G, Mehl GH, Welch C, Cruickshank E, Strachan GJ, et al. Temperature dependence of bend elastic constant in oblique helicoidal cholesterics. Phys Rev Res. 2020;2:013248.
65. Joshi V, Paterson DA, Storey JMD, Imrie CT, Chien LC. Tunable backflow in chiral nematic liquid crystals via twist-bend nematogens and surface-localised &ITin&IT-&ITsitu &ITpolymer protrusions. Liq Cryst. 2017;44:2327-2336.
66. Mandle RJ, Davis EJ, Archbold CT, Cowling SJ, Goodby JW. Microscopy studies of the nematic NTB phase of 1,11-di-(1 ''-cyanobipheny1-4-yOundecane. J Mater Chem C. 2014;2:556-566.
67. Paterson DA, Abberley JP, Harrison WT, Storey JM, Imrie CT. Cyanobiphenyl-based liquid crystal dimers and the twist-bend nematic phase. Liq Cryst. 2017;44:127-146.
68. Paterson DA, Walker R, Storey JMD, Imrie CT. Molecular structure and the twist-bend nematic phase: the role of spacer length in liquid crystal dimers. Liq Cryst. 2023;50:725-736.
69. Ramou E, Welch C, Hussey J, Ahmed Z, Karahaliou PK, Mehl GH. The induction of the N-tb phase in mixtures. Liq Cryst. 2018;45:1929-1935.
70. Arakawa Y, Arai Y, Horita K, Komatsu K, Tsuji H. Twist-Bend Nematic Phase Behavior of Cyanobiphenyl-Based Dimers with Propane, Ethoxy, and Ethylthio Spacers. Crystals. 2022;12:1734.
71. Luckhurst GR. Liquid crystals: a chemical physicist's view. Liq Cryst. 2005;32:1335-1364.
72. Emsley JW, Luckhurst GR, Shilstone GN, Sage I. The preparation and properties of the alpha,omega-bis(4,4'-cyanobiphenyloxy)alkanes - nematogenic molecules with a flexible core. Molec Cryst Liq Cryst. 1984;102:223-233.
73. Babakhanova G, Parsouzi Z, Paladugu S, Wang H, Nastishin YA, Shiyanovskii SV, et al. Elastic and viscous properties of the nematic dimer CB7CB. Phys Rev E. 2017;96:062704.
74. Cestari M, Frezza E, Ferrarini A, Luckhurst GR. Crucial role of molecular curvature for the bend elastic and flexoelectric properties of liquid crystals: mesogenic dimers as a case study. J Mater Chem. 2011;21:12303-12308.
75. Xiang J, Shiyanovskii SV, Imrie CT, Lavrentovich OD. Electrooptic Response of Chiral Nematic Liquid Crystals with Oblique Helicoidal Director. Phys Rev Lett. 2014;112:217801.
76. Xiang J, Li YN, Li Q, Paterson DA, Storey JMD, Imrie CT, et al. Electrically Tunable Selective Reflection of Light from Ultraviolet to Visible and Infrared by Heliconical Cholesterics. Adv Mater. 2015;27:3014-3018.
77. Iadlovska OS, Thapa K, Rajabi M, Shiyanovskii SV, Lavrentovich OD. In situ measurements of twist and bend elastic constants in the oblique helicoidal cholesteric. Phys Rev E. 2022;106:024702.
78. DeGennes PG. Calculation of distortion in a cholesterol structure by a magnetic field. Solid State Commun. 1968;6:163-165.
79. Meyer RB. Effects of electric and magnetic fields on structure of cholesteric liquid crystals. Appl Phys Lett. 1968;12:281-282.
80. Miyaura N, Yanagi T, Suzuki A. The palladium-catalyzed cross-coupling reaction of phenylboronic acid with haloarenes in the presence of bases. Synth Commun. 1981;11:513-519.

81. Kanagarajan V, Thanusu J, Gopalakrishnan M. Synthesis and in vitro microbiological evaluation of an array of biolabile 2-morpholino-N-(4,6-diarylpyrimidin-2-yl)acetamides. Eur J Med Chem. 2010;45:1583-1589.
82. Obaza J, Smith FX. A malonic ester synthesis with acid-chlorides - the homologation of dioic acids. Synth Commun. 1982;12:19-23.
83. Frisch MJ, Trucks GW, Schlegel HB, Scuseria GE, Robb MA, Cheeseman JR, et al. Gaussian 09 (Revision D.01). Wallingford CT: Gaussian Inc.; 2016.
84. Dennington R, Keith T, Millam J. Gauss View, Version 5. 2009:Shawnee Mission, KS, Semichem Inc.
85. Tarini M, Cignoni P, Montani C. Ambient occlusion and edge cueing to enhance real time molecular visualization. IEEE Trans Vis Comp Graphics. 2006;12:1237-1244.
86. Kedzierski J, Raszewski Z, Kojdecki MA, Kruszelnicki-Nowinowski E, Perkowski P, Piecek W, et al. Determination of ordinary and extraordinary refractive indices of nematic liquid crystals by using wedge cells. Opto-Electron Rev. 2010;18:214-218.
87. Nastishin YA, Polak RD, Shiyanovskii SV, Bodnar VH, Lavrentovich OD. Nematic polar anchoring strength measured by electric field techniques. J Appl Phys. 1999;86:4199-4213.
88. Salamonczyk M, Vaupotic N, Pociecha D, Wang C, Zhu CH, Gorecka E. Structure of nanoscale-pitch helical phases: blue phase and twist-bend nematic phase resolved by resonant soft X-ray scattering. Soft Matter. 2017;13:6694-6699.
89. Saha R, Feng C, Welch C, Mehl GH, Feng J, Zhu C, et al. The interplay between spatial and heliconical orientational order in twist-bend nematic materials. Phys Chem Chem Phys. 2021;23:4055-4063.
90. Arakawa Y, Komatsu K, Feng J, Zhu CH, Tsuji H. Distinct twist-bend nematic phase behaviors associated with the ester-linkage direction of thioether-linked liquid crystal dimers. Mater Adv. 2021;2:261-272.
91. Humphries RL, Luckhurst GR. Statistical-theory of liquid-crystalline mixtures - components of different size. Chem Phys Lett. 1973;23:567-570.
92. Arakawa Y, Horita K, Igawa K. Phase behaviour of ester-linked cyanobiphenyl dimers and fluorinated analogues: the direct isotropic to twist-bend nematic phase transition. Liq Cryst. 2023:2216-2228.
93. Wang DL, Liu J, Zhao WG, Zeng YM, Huang JJ, Fang JL, et al. Facile Synthesis of Liquid Crystal Dimers Bridged with a Phosphonic Group. Chem Eur J. 2022;28: e2022021.
94. Challa PK, Borshch V, Parri O, Imrie CT, Sprunt SN, Gleeson JT, et al. Twist-bend nematic liquid crystals in high magnetic fields. Phy Rev E. 2014;89:060501.
95. Parsouzi Z, Pardaev SA, Welch C, Ahmed Z, Mehl GH, Baldwin AR, et al. Light scattering study of the "pseudo-layer'' compression elastic constant in a twist-bend nematic liquid crystal. Phys Chem Chem Phys. 2016;18:31645-31652.
96. Sarkar P, Mandal P, Paul S, Paul R, Dabrowski R, Czuprynski K. X-ray diffraction, optical birefringence, dielectric and phase transition properties of the long homologous series of nematogens 4-(*trans*-4'-*n*-alkylcyclohexyl) isothiocyanatobenzenes. Liq Cryst. 2003;30:507-527.
97. Imrie CT, Henderson PA. Liquid crystal dimers and higher oligomers: Between monomers and polymers. Chem Soc Rev. 2007;36:2096-2124.
98. Babakhanova G, Wang H, Rajabi M, Li D, Li Q, Lavrentovich OD. Elastic and electro-optical properties of flexible fluorinated dimers with negative dielectric anisotropy. Liq Cryst. 2022;49:982-994.

99. Meyer C, Luckhurst GR, Dozov I. The temperature dependence of the heliconical tilt angle in the twist-bend nematic phase of the odd dimer CB7CB. J Mater Chem C. 2015;3:318-328.
100. Cukrov G, Golestani YM, Xiang J, Nastishin YA, Ahmed Z, Welch C, et al. Comparative analysis of anisotropic material properties of uniaxial nematics formed by flexible dimers and rod-like monomers. Liq Cryst. 2017;44:219-231.
101. Pociecha D, Crawford CA, Paterson DA, Storey JMD, Imrie CT, Vaupotic N, et al. Critical behavior of the optical birefringence at the nematic to twist-bend nematic phase transition. Phys Rev E. 2018;98:052706.
102. Adlem K, Copic M, Luckhurst GR, Mertelj A, Parri O, Richardson RM, et al. Chemically induced twist-bend nematic liquid crystals, liquid crystal dimers, and negative elastic constants. Phys Rev E. 2013;88:022503.
103. Greco C, Luckhurst GR, Ferrarini A. Molecular geometry, twist-bend nematic phase and unconventional elasticity: a generalised Maier-Saupe theory. Soft Matter. 2014;10:9318-9323.
104. Henderson PA, Niemeyer O, Imrie CT. Methylene-linked liquid crystal dimers. Liq Cryst. 2001;28:463-472.
105. Henderson PA, Seddon JM, Imrie CT. Methylene- and ether-linked liquid crystal dimers II. Effects of mesogenic linking unit and terminal chain length. Liq Cryst. 2005;32:1499-1513.
106. Emerson APJ, Luckhurst GR. On the relative propensities of ether and methylene linkages for liquid-crystal formation in calamitics. Liq Cryst. 1991;10:861-868.
107. Ferrarini A, Luckhurst GR, Nordio PL, Roskilly SJ. Understanding the dependence of the transitional properties of liquid crystal dimers on their molecular geometry. Liq Cryst. 1996;21:373-382.
108. Ferrarini A, Luckhurst GR, Nordio PL, Roskilly SJ. Prediction of the transitional properties of liquid-crystal dimers - a molecular-field calculation based on the surface tensor parametrization. J Chem Phys. 1994;100:1460-1469.